

AN SZ-SELECTED SAMPLE OF THE MOST MASSIVE GALAXY CLUSTERS IN THE 2500-SQUARE-DEGREE SOUTH POLE TELESCOPE SURVEY

R. WILLIAMSON^{1,2}, B. A. BENSON^{1,3}, F. W. HIGH^{1,2}, K. VANDERLINDE⁴, P. A. R. ADE⁵, K. A. AIRD⁶, K. ANDERSSON^{7,8}, R. ARMSTRONG⁹, M. L. N. ASHBY¹⁰, M. BAUTZ⁸, G. BAZIN^{7,11}, E. BERTIN¹², L. E. BLEEM^{1,13}, M. BONAMENTE¹⁴, M. BRODWIN¹⁰, J. E. CARLSTROM^{1,2,3,13,15}, C. L. CHANG^{1,3,15}, S. C. CHAPMAN¹⁶, A. CLOCCHIATTI¹⁷, T. M. CRAWFORD^{1,2}, A. T. CRITES^{1,2}, T. DE HAAN⁴, S. DESAI^{9,18}, M. A. DOBBS⁴, J. P. DUDLEY⁴, G. G. FAZIO¹⁰, R. J. FOLEY¹⁰, W. R. FORMAN¹⁰, G. GARMIRE¹⁹, E. M. GEORGE²⁰, M. D. GLADDERS^{1,2}, A. H. GONZALEZ²¹, N. W. HALVERSON²², G. P. HOLDER⁴, W. L. HOLZAPFEL²⁰, S. HOOVER^{1,3}, J. D. HRUBES⁶, C. JONES¹⁰, M. JOY¹⁴, R. KEISLER^{1,13}, L. KNOX²³, A. T. LEE^{20,24}, E. M. LEITCH^{1,2}, M. LUEKER²⁰, D. LUONG-VAN⁶, D. P. MARRONE^{1,6}, J. J. McMAHON^{1,3,25}, J. MEHL^{1,2}, S. S. MEYER^{1,2,3,13}, J. J. MOHR^{7,11,26}, T. E. MONTROY²⁷, S. S. MURRAY¹⁰, S. PADIN^{1,2,28}, T. PLAGGE^{1,2}, C. PRYKE^{1,2,3}, C. L. REICHARDT²⁰, A. REST^{29,30}, J. RUEL²⁹, J. E. RUHL²⁷, B. R. SALIWANCHIK²⁷, A. SARO⁷, K. K. SCHAFFER^{1,3,31}, L. SHAW^{4,32}, E. SHIROKOFF²⁰, J. SONG²⁵, H. G. SPIELER²⁴, B. STALDER¹⁰, S. A. STANFORD²³, Z. STANISZEWSKI²⁷, A. A. STARK¹⁰, K. STORY^{1,13}, C. W. STUBBS^{29,10}, J. D. VIEIRA^{1,13,28}, A. VIKHLININ¹⁰, AND A. ZENTENO^{7,11}

Accepted by *ApJ*

ABSTRACT

The South Pole Telescope (SPT) is currently surveying 2500 deg² of the southern sky to detect massive galaxy clusters out to the epoch of their formation using the Sunyaev-Zel'dovich (SZ) effect. This paper presents a catalog of the 26 most significant SZ cluster detections in the full survey region. The catalog includes 14 clusters which have been previously identified and 12 that are new discoveries. These clusters were identified in fields observed to two differing noise depths: 1500 deg² at the final SPT survey depth of 18 μ K-arcmin at 150 GHz, and 1000 deg² at a depth of 54 μ K-arcmin. Clusters were selected on the basis of their SZ signal-to-noise ratio (S/N) in SPT maps, a quantity which has been demonstrated to correlate tightly with cluster mass. The S/N thresholds were chosen to achieve a comparable mass selection across survey fields of both depths. Cluster redshifts were obtained with optical and infrared imaging and spectroscopy from a variety of ground- and space-based facilities. The redshifts range from $0.098 \leq z \leq 1.132$ with a median of $z_{\text{med}} = 0.40$. The measured SZ S/N and redshifts lead to unbiased mass estimates ranging from $9.8 \times 10^{14} M_{\odot} h_{70}^{-1} \leq M_{200}(\rho_{\text{mean}}) \leq 3.1 \times 10^{15} M_{\odot} h_{70}^{-1}$. Based on the SZ mass estimates, we find that none of the clusters are individually in significant tension with the Λ CDM cosmological model. We also test for evidence of non-Gaussianity based on the cluster sample and find the data show no preference for non-Gaussian perturbations.

Subject headings: galaxies: clusters: individual, cosmology: observations

Electronic address: rw247@kicp.uchicago.edu

¹ Kavli Institute for Cosmological Physics, University of Chicago, 5640 South Ellis Avenue, Chicago, IL 60637

² Department of Astronomy and Astrophysics, University of Chicago, 5640 South Ellis Avenue, Chicago, IL 60637

³ Enrico Fermi Institute, University of Chicago, 5640 South Ellis Avenue, Chicago, IL 60637

⁴ Department of Physics, McGill University, 3600 Rue University, Montreal, Quebec H3A 2T8, Canada

⁵ Department of Physics and Astronomy, Cardiff University, CF24 3YB, UK

⁶ University of Chicago, 5640 South Ellis Avenue, Chicago, IL 60637

⁷ Department of Physics, Ludwig-Maximilians-Universität, Scheinerstr. 1, 81679 München, Germany

⁸ MIT Kavli Institute for Astrophysics and Space Research, Massachusetts Institute of Technology, 77 Massachusetts Avenue, Cambridge, MA 02139

⁹ National Center for Supercomputing Applications, University of Illinois, 1205 West Clark Street, Urbana, IL 61801

¹⁰ Harvard-Smithsonian Center for Astrophysics, 60 Garden Street, Cambridge, MA 02138

¹¹ Excellence Cluster Universe, Boltzmannstr. 2, 85748 Garching, Germany

¹² Institut d'Astrophysique de Paris, UMR 7095 CNRS, Université Pierre et Marie Curie, 98 bis boulevard Arago, F-75014 Paris, France

¹³ Department of Physics, University of Chicago, 5640 South Ellis Avenue, Chicago, IL 60637

¹⁴ Department of Space Science, VP62, NASA Marshall Space Flight Center, Huntsville, AL 35812

¹⁵ Argonne National Laboratory, 9700 S. Cass Avenue, Argonne, IL, USA 60439

¹⁶ Institute of Astronomy, Madingley Road, Cambridge, CB3 0HA, U.K.

¹⁷ Departamento de Astronomía y Astrofísica, PUC Casilla 306, Santiago 22, Chile

¹⁸ Department of Astronomy, University of Illinois, 1002 West Green Street, Urbana, IL 61801

¹⁹ Department of Astronomy and Astrophysics, Pennsylvania State University, 525 Davey Lab, University Park, PA 16802

²⁰ Department of Physics, University of California, Berkeley, CA 94720

²¹ Department of Astronomy, University of Florida, Gainesville, FL 32611

²² Department of Astrophysical and Planetary Sciences and Department of Physics, University of Colorado, Boulder, CO 80309

²³ Department of Physics, University of California, One Shields Avenue, Davis, CA 95616

²⁴ Physics Division, Lawrence Berkeley National Laboratory, Berkeley, CA 94720

²⁵ Department of Physics, University of Michigan, 450 Church Street, Ann Arbor, MI, 48109

²⁶ Max-Planck-Institut für extraterrestrische Physik, Giessenbachstr. 85748 Garching, Germany

²⁷ Physics Department and CERCA, Case Western Reserve University, 10900 Euclid Ave., Cleveland, OH 44106

²⁸ California Institute of Technology, 1200 E. California Blvd., Pasadena, CA 91125

²⁹ Department of Physics, Harvard University, 17 Oxford Street, Cambridge, MA 02138

³⁰ Space Telescope Science Institute, 3700 San Martin Dr., Bal-

1. INTRODUCTION

Galaxy clusters are the most massive collapsed objects in the Universe, with masses that range from $10^{14} M_{\odot}$ to over $10^{15} M_{\odot}$. Their abundance as a function of mass and redshift can be used to constrain cosmological parameters (Wang & Steinhardt 1998; Haiman et al. 2001; Holder et al. 2001; Batty & Weller 2003; Molnar et al. 2004; Wang et al. 2004; Lima & Hu 2007), and this constraining power has now been demonstrated with real cluster samples identified in optical (e.g., Rozo et al. 2010), X-ray (e.g., Vikhlinin et al. 2009b), and, most recently, millimeter (mm) (Vanderlinde et al. 2010; Sehgal et al. 2010b) data. The most massive clusters are of particular interest, especially at high redshifts. As tracers of the most extreme tails of the cosmological density field, these clusters can be used to place limits on the Gaussianity of the initial density perturbations of the Universe (e.g., Matarrese et al. 2000). Furthermore, massive, high-redshift clusters provide laboratories for the study of astrophysics (particularly galaxy formation and evolution) in dense environments in the early Universe.

Although the largest existing catalogs of galaxy clusters are derived from optical and X-ray observations, clusters can also be identified by their interaction with cosmic microwave background (CMB) photons. The thermal Sunyaev-Zel'dovich (SZ) effect is a spectral distortion of the CMB caused by inverse-Compton scattering with hot cluster gas (Sunyaev & Zel'dovich 1972). The surface brightness of the effect is independent of redshift, and the integrated thermal SZ effect from a cluster is expected to trace cluster mass with low scatter (Barbosa et al. 1996; Holder & Carlstrom 2001; Motl et al. 2005; Nagai et al. 2007; Stanek et al. 2009), implying that SZ cluster surveys should deliver nearly mass-limited catalogs of clusters to arbitrarily high redshift. With the recent development of bolometric receivers with hundreds or thousands of pixels, dedicated mm-wave SZ surveys over large areas of the sky are now being carried out by the South Pole Telescope (SPT, Carlstrom et al. 2011) and the Atacama Cosmology Telescope (ACT, Fowler et al. 2007). Such surveys promise to be powerful tools for cluster cosmology.

The SPT is currently surveying 2500 deg^2 of the southern sky at 95, 150, and 220 GHz. To date, roughly 1500 deg^2 have been observed to a depth of $18 \mu\text{K-arcmin}$ at 150 GHz.³³ Motivated by preliminary evidence of surprisingly massive, high-redshift clusters in these first 1500 deg^2 , we conducted “preview” observations of the remaining $\sim 1000 \text{ deg}^2$ of the SPT survey field during a three week period of the 2010 Austral winter, mapping this region to a noise level three times higher than the full survey depth ($54 \mu\text{K-arcmin}$ at 150 GHz). In this paper, we present a catalog of the 26 most significant galaxy clusters in the full 2500 deg^2 SPT survey field and test whether the cluster masses and redshift distribution are consistent with those expected in a ΛCDM cosmology.

timore, MD 21218

³¹ Liberal Arts Department, School of the Art Institute of Chicago, 112 S Michigan Ave, Chicago, IL 60603

³² Department of Physics, Yale University, P.O. Box 208210, New Haven, CT 06520-8120

³³ In this work, “ $\mu\text{K-arcmin}$ ” refers to the rms noise in equivalent CMB fluctuation temperature in a map with square $1' \times 1'$ pixels.

We complement our SZ cluster catalog with data from observations at other wavelengths. Spectroscopic or photometric redshifts were obtained for each cluster as a part of a dedicated optical and infrared (IR) follow-up campaign. X-ray luminosities were also determined for each cluster using a combination of pointed observations with the *Chandra* satellite and measurements from the *Roentgensatellit* (ROSAT) mission (Voges et al. 1999).

This paper is presented as follows: Section 2 describes the SPT observations, data reduction pipeline, and cluster-finding methodology. The catalog is presented in Section 3. Section 4 introduces the simulations carried out to test purity and completeness, and to determine the scaling between the observable quantity (signal-to-noise ratio, S/N) and cluster mass. Section 5 describes the optical and IR follow-up measurements used to determine the cluster redshifts, and Section 6 presents X-ray luminosities for these clusters. Cosmological implications of this cluster catalog are discussed in Section 7, and our conclusions are presented in Section 8.

Unless otherwise noted, we have assumed a WMAP7+BAO+ H_0 ΛCDM cosmology (Komatsu et al. 2011) with $\Omega_M = 0.272$, $\Omega_{\Lambda} = 0.728$ and $H_0 = 70.2 \text{ km s}^{-1} \text{ Mpc}^{-1}$ with distance measurements from Baryon Acoustic Oscillations (BAO) in the distribution of galaxies (Percival et al. 2010) and the Hubble constant (H_0) measurement from Riess et al. (2009). Cluster mass estimates are reported in terms of $M_{200}(\rho_{\text{mean}})$, the mass enclosed within a radius corresponding to an average density of 200 times the mean density of the Universe. For the purposes of comparison with certain scaling relations in the literature, we also convert these masses into $M_{500}(\rho_{\text{crit}})$, or the mass enclosed within a radius corresponding to an average density of 500 times the critical density. The conversion factor for each cluster is calculated assuming a Navarro-Frenk-White density profile and the mass-concentration relation of Duffy et al. (2008).

2. INSTRUMENT, OBSERVATIONS, AND DATA REDUCTION

2.1. The South Pole Telescope

The SPT, a 10-meter off-axis Gregorian design with a 1 deg^2 field of view, has been searching for galaxy clusters in the mm-wave sky since its commissioning in 2007. The SPT is located within 1 km of the geographical South Pole. At an altitude of 2800 meters above sea level, the South Pole is one of the premier locations for mm-wave astronomy. The high altitude and low temperatures ensure an atmosphere with low water-vapor content and excellent transparency. Meanwhile, the location near the Earth’s rotational axis allows 24-hour access to the target fields.

The SZ receiver currently mounted on the telescope consists of 960 transition-edge-sensor bolometers (Lee et al. 1998), cooled to a temperature of 280 mK. These bolometers are split into six wedges each containing 160 detectors. The sensitivity and configuration of these wedges have changed over the four years of scientific operation. In 2007, we fielded a preliminary array with wedges at all three frequencies but with limited sensitivity. In 2008, the array contained a single 95 GHz wedge, three 150 GHz wedges and two 220 GHz wedges. The

95 GHz wedge did not produce science-quality data, but the 150 and 220 GHz wedges performed to specification. In 2009, the 95 GHz wedge was replaced with a wedge with much higher sensitivity, and one of the 220 GHz wedges was replaced by a 150 GHz wedge, resulting in an array with one wedge at 95 GHz, four wedges at 150 GHz, and one wedge at 220 GHz. The focal plane configuration has remained the same since 2009. The 10-meter primary is conservatively illuminated, resulting in beam sizes (FWHM) of approximately 1.6', 1.1', and 1.0' at 95, 150, and 220 GHz.

The SPT team has previously published two SZ-selected cluster samples: Staniszewski et al. (2009, hereafter S09) presented four clusters (including three newly discovered clusters) selected from ~ 40 deg 2 of 2007 and 2008 150 GHz data, while Vanderlinde et al. (2010, hereafter V10) presented 21 clusters (including 12 new discoveries beyond S09) selected from 150 GHz data in the full 200 deg 2 of 2008 observations.

2.2. Observations

The SPT-SZ survey area is a contiguous 2500 deg 2 region defined by the boundaries 20h \leq R.A. \leq 24h; 0h \leq R.A. \leq 7h and $-65^\circ \leq \delta \leq -40^\circ$. This region comprises the majority of the low-dust-emission southern sky below $\delta = -40^\circ$. Observing fields north of this declination becomes difficult with the SPT because of the increased atmospheric loading and attenuation at low elevation. We split the survey region into 19 fields, ranging in size from ~ 70 deg 2 to ~ 230 deg 2 . Single observations of fields of this size can be completed in an hour or two, allowing a regular schedule of interleaved calibrations (see S09 and Carlstrom et al. (2011) for details). The exact size, shape, location, and order of observation of these fields are determined by a combination of factors including availability of data at other wavelengths, sun avoidance (some of our observations take place during the Austral spring and summer), and the desire to have a final survey area that is easy to define. The location, year of observation and size for each field are shown in Table 1. Figure 1 shows the full survey region and the individual field borders overlaid on the 100 μ m dust map from Schlegel et al. (1998).

The standard operating mode of the SPT is to observe a target field by scanning back and forth in azimuth across the field followed by a step in elevation. These steps are large compared to the beam size, so subsequent observations of the field have a small offset in elevation applied in order to oversample the sky. Certain fields were observed in what is called a “lead-trail” mode. In this observing mode, the lead half of a field was scanned followed by the trail half, as opposed to scanning the entire azimuth range of the field in a single scan. This strategy was employed to safeguard against possible ground contamination, but we see no evidence of such contamination on the angular scales of interest to this work. Approximately two-thirds of the ra21hdec-50 observations³⁴ were taken using an elevation scan mode rather than scanning in azimuth. In this mode, the telescope was parked at a fixed azimuth and scanned up and down in elevation, allowing the sky to drift through the

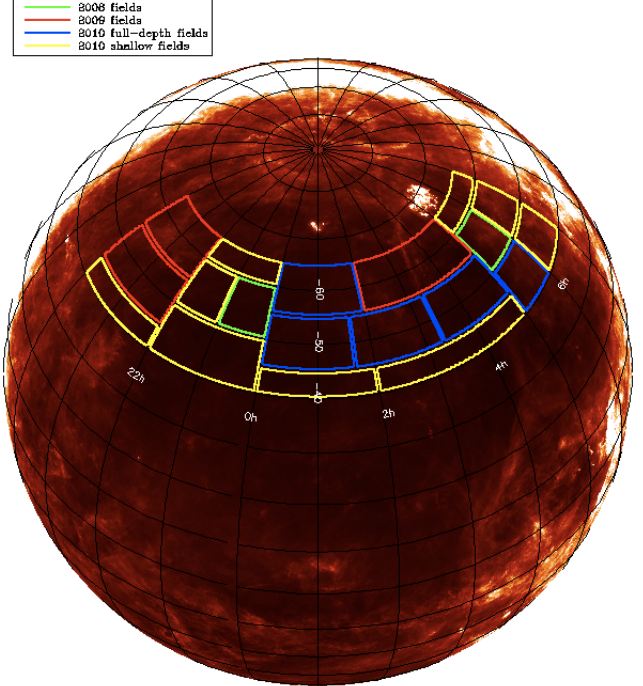


FIG. 1.— Outlines of the SPT-SZ survey fields overlaid on an orthographic projection of the IRAS 100 μ m dust map from Schlegel et al. (1998). The sky is rotated such that the South Celestial Pole is at the top of the globe, and R.A. = 1h faces the viewer. Green lines indicate fields observed in 2008, red lines indicate fields observed in 2009, blue lines indicate fields observed to full depth in 2010, and yellow lines indicate fields observed to preview depth in 2010, which will be completed to full depth in 2011.

field of view. We include data from both azimuth and elevation scans on this field. We have investigated the effects of these different scan strategies on noise properties and cluster finding and found these effects to be negligible.

As mentioned in the introduction, observations have been completed to full survey depth (a noise level of 18 μ K-arcmin at 150 GHz) for roughly 1500 deg 2 of the SPT survey region. Initial preview observations of the remaining ~ 1000 deg 2 were performed in late 2010, to a noise level of 54 μ K-arcmin at 150 GHz, or three times the full-depth noise level. The results presented in this work are based on data from both the full-depth and preview-depth fields.

One field, the ra23h30dec-55 field, was observed in both 2008 and 2010. Given the higher quality of the 95 GHz wedge in 2010, that year’s data is used in preference to the 2008 data, which was used in V10. For this reason, the properties of SPT-CL J2337-5942 are not identical to those reported in V10. We choose not to combine the 2008 and 2010 data in order to reduce the number of different map depths considered.

2.3. Data processing, calibration, and map-making

The data reduction pipeline applied to the SPT data is very similar to that described in previous SPT papers such as S09, V10, and Shirokoff et al. (2011). An overview of the processing is presented here, highlighting differences with earlier SPT releases. The same data-processing and map-making procedure is used for each

³⁴ Coordinates in the field names refer to the R.A. and δ of the center of the field.

TABLE 1
2008-2011 SPT FIELDS

| Field Name | Obs Year | Area [deg ²] |
|----------------|----------|--------------------------|
| ra5h30dec-55 | 2008 | 90 |
| ra3h30dec-60 | 2009 | 230 |
| ra21hdec-50 | 2009 | 200 |
| ra21hdec-60 | 2009 | 150 |
| ra0h50dec-50 | 2010 | 160 |
| ra1hdec-60 | 2010 | 150 |
| ra2h30dec-50 | 2010 | 160 |
| ra4h10dec-50 | 2010 | 160 |
| ra5h30dec-45 | 2010 | 110 |
| ra23h30dec-55 | 2010* | 100 |
| ra1hdec-42.5 | 2010S | 110 |
| ra3h30dec-42.5 | 2010S | 170 |
| ra6hdec-62.5 | 2010S | 70 |
| ra6h30dec-45 | 2010S | 110 |
| ra6h30dec-55 | 2010S | 90 |
| ra21hdec-42.5 | 2010S | 110 |
| ra22h30dec-55 | 2010S | 80 |
| ra23hdec-45 | 2010S | 210 |
| ra23hdec-62.5 | 2010S | 70 |

NOTE. — The field centers, year of observation and area of the SPT fields. The 19 SPT fields cover a total of roughly 2500 deg². The nominal noise level of an SPT field is 18 μ K-arcmin. “2010S” refers to those fields observed to three times the survey noise level (54 μ K-arcmin). The ra23h30dec-55 field was also observed in 2008, but only the 2010 data is used in this work.

field, with minor adaptations in filtering to produce uniform map properties regardless of scan strategy.

The first steps in processing are to flag regions of compromised data (for instance, time samples with cosmic ray events) and to reconstruct the pointing for each detector. We then calibrate the time-ordered data (TOD) to CMB temperature units. As in S09, this calibration is based on observations of a galactic HII region (RCW38). The TOD is filtered and co-added into the final single-frequency map with inverse-noise weighting.

The filtering consists of bandpass filtering the TOD and removing correlated noise between detectors. The high-pass filter is implemented by removing a ninth-order Legendre polynomial and a set of Fourier modes from each scan. The highest-frequency Fourier modes removed correspond to an angular frequency of $k = 400$ in the scan direction.³⁵ Depending on the scan strategy used for the observation, this filter acts as a high-pass filter in the R.A. or decl. direction. This differs slightly from V10 where only a first-order polynomial was removed, and the set of Fourier modes removed was defined by temporal frequency ($f < .25$ Hz) rather than angular frequency ($k < 400$). The cutoff definition was altered to handle variable scan speeds. For the 2008 scan speeds, 0.25 Hz corresponds to $k \simeq 360$, which means that the k -space high-pass cutoff is slightly higher in this work than in V10. A low-pass filter was also applied (with a cutoff at $k \sim 30000$) to avoid aliasing of high-frequency TOD noise when the data is binned into a map.

Atmospheric noise is correlated across the entire focal plane. V10 removed the mean and slope across all detectors in a frequency band at each time sample. However,

the number of detectors at the two frequencies used in this work (95 and 150 GHz) differ by a factor of four, so this scheme would filter different spatial modes on the sky at each frequency. Instead, as was done in Shirokoff et al. (2011), the mean of the TOD across a geometrically compact set of one quarter of the 150 GHz detectors or all the 95 GHz detectors (i.e., across one detector wedge) is subtracted at each time sample. This acts as an isotropic high-pass filter with a cutoff at roughly $k = 500$.

2.4. Cluster Finding

As discussed in Section 2.2, most of the SPT fields have been observed in three frequency bands, centered at 95, 150, and 220 GHz. Multiple sky signals and sources of noise contribute to each single-frequency co-added map of a field, and each of these contributions has unique spatial and spectral properties. Primary CMB fluctuations, emissive point sources, and noise (both atmospheric and instrumental) contribute to the maps at all three frequencies. A small signal from the kinetic SZ (kSZ) effect (due to the interaction between CMB photons and free electrons with a bulk velocity) also contributes to all three frequencies. Most importantly for this work, the 95 GHz and 150 GHz maps contain an additional signal due to the thermal SZ (tSZ) effect from clusters. Because we can predict the spectral signature of the tSZ effect (up to a small relativistic correction), we can combine the maps from the three bands to maximize sensitivity to tSZ and minimize noise and other contaminants. Furthermore, we can use the fact that the galaxy clusters we expect to find have a different spatial profile than other signals and noise to construct a spatial filter that maximizes sensitivity to cluster-shaped signals.

As shown by Melin et al. (2006) and others, the optimal³⁶ way to extract a cluster-shaped tSZ signal from our data is to construct a simultaneous spatial-spectral filter. We begin by assuming that the maps are fully described by

$$T(\mathbf{x}, \nu_i) = B(\mathbf{x}, \nu_i) * [f_{\text{sz}}(\nu_i)T_{\text{CMB}}y_{\text{sz}}(\mathbf{x}) + n_{\text{astro}}(\mathbf{x}, \nu_i)] + n_{\text{noise}}(\mathbf{x}, \nu_i), \quad (1)$$

where y_{sz} is the true tSZ sky signal in units of the Compton y parameter, T_{CMB} is the mean temperature of the CMB, f_{sz} encodes the frequency scaling of the tSZ effect relative to primary CMB fluctuations (e.g., Carlstrom et al. 2002), n_{astro} and n_{noise} are the astrophysical signals and instrument/atmospheric noise we wish to de-weight, $B(\mathbf{x}, \nu_i)$ encodes the instrument beam and any filtering applied in the analysis, and “*” denotes convolution. Given this assumption, the matched spatial-spectral filter is given by

$$\psi(k_x, k_y, \nu_i) = \sigma_{\psi}^{-2} \sum_j \mathbf{N}_{ij}^{-1}(k_x, k_y) f_{\text{sz}}(\nu_j) S_{\text{filt}}(k_x, k_y, \nu_j). \quad (2)$$

³⁶ This method is in fact optimal only under certain assumptions, the most important of which are that all sources of noise and unwanted astrophysical signals are random and translationally invariant, and that the exact spectral and spatial behavior of every component of signal and noise are known perfectly.

³⁵ We use the flat-sky approximation throughout this work, so $|\mathbf{k}| \equiv \ell$.

Here, σ_ψ^{-2} is the predicted variance in the filtered map

$$\sigma_\psi^{-2} = \sum_{i,j} f_{\text{sz}}(\nu_i) S_{\text{filt}}(k_x, k_y, \nu_i) \mathbf{N}_{ij}^{-1}(k_x, k_y) \times \quad (3)$$

$$f_{\text{sz}}(\nu_j) S_{\text{filt}}(k_x, k_y, \nu_j),$$

and S_{filt} is the assumed cluster profile convolved with $B(\mathbf{x}, \nu_i)$. The k_x and k_y arguments are included explicitly in S_{filt} because, while the underlying cluster profile is assumed to be azimuthally symmetric, the filtering described in Section 2.3 is anisotropic. The ν argument is included explicitly to account for the fact that the filtering and instrument beam can be different in the different SPT bands. \mathbf{N} is the band-band, pixel-pixel covariance matrix describing the noise and non-tSZ signal

$$\mathbf{N}_{abij} = \quad (4)$$

$$\langle [B(\mathbf{x}_a, \nu_i) * n_{\text{astro}}(\mathbf{x}_a, \nu_i) + n_{\text{noise}}(\mathbf{x}_a, \nu_i)]$$

$$[B(\mathbf{x}_b, \nu_j) * n_{\text{astro}}(\mathbf{x}_b, \nu_j) + n_{\text{noise}}(\mathbf{x}_b, \nu_j)] \rangle.$$

Under the assumption that these components are translationally invariant, the pixel-pixel part of this matrix will be diagonal in the Fourier domain, which is why we only include the band indices in Equation 2. This also means that ψ can be evaluated separately at each value of $\{k_x, k_y\}$, and the largest matrix that needs to be inverted is $N_{\text{bands}}\text{-by-}N_{\text{bands}}$.

There should be no correlation between the astrophysical signals and instrumental/atmospheric noise, in which case \mathbf{N} can be separated into $\mathbf{N}_{\text{astro}}$ and $\mathbf{N}_{\text{noise}}$. Furthermore, the instrumental noise should be uncorrelated between bands, although the atmospheric noise may have correlations. We have performed correlation analyses on SPT maps similar to those used in this work and found little, if any, noise correlation between bands, which is expected because the correlated part of the atmospheric emission is largely removed in the filtering described in Section 2.3. In this case, we can estimate $\mathbf{N}_{\text{noise}}$ individually in each band. We do so using the jackknife procedure described in V10 and S09.

Our model for $\mathbf{N}_{\text{astro}}$ is a combination of primary and lensed CMB fluctuations, point sources below the SPT detection threshold, kSZ, and tSZ from clusters below the SPT detection threshold. The power-spectrum shapes and 150 GHz amplitudes for these components are identical to those used in V10. The spectral behavior of the primary CMB, kSZ, and tSZ components are known (up to the relativistic correction for tSZ, which we ignore). The spectral behavior of the point sources is assumed to be such that the flux density of a given source follows a power law in frequency $(\nu/\nu_0)^\alpha$, with $\alpha = 3.6$. This is consistent with the behavior of dusty, star-forming galaxies (DSFGs) below the SPT detection threshold. Radio sources below the SPT detection threshold are expected to contribute negligibly to the map rms compared to noise (Hall et al. 2010; Shirokoff et al. 2011).

As in V10 and S09, the source template S is described by a projected spherical β -model, with β fixed to 1,

$$\Delta T = \Delta T_0 (1 + \theta^2/\theta_c^2)^{-1}, \quad (5)$$

where the normalization ΔT_0 and the core radius θ_c are free parameters. As in V10 and S09, twelve different matched filters were constructed and applied to the data,

each with a different core radius, spaced evenly between $0.25'$ and $3.0'$. As in V10, point sources detected above 5σ were masked out to a radius of $4'$, with the value inside that radius set to the average of the surrounding pixels. For extended sources, a custom mask was applied, covering the shape of the emission. In both cases, cluster detections inside the masked region or within $4'$ of the outer edge of the masked region were rejected, meaning that any detection within $8'$ of a masked point source was rejected.

The method of extracting clusters from the filtered maps in this work (including S/N estimation and peak detection) is identical to that used in V10. As in V10, we refer to the detection significance maximized across all twelve matched filters as ξ , and we use ξ as the primary SZ observable.

We have measured the performance of the multi-band cluster detection algorithm relative to single-band detection and found significant improvement when we add the 95 GHz data—which has roughly a factor of two higher noise in CMB fluctuation temperature than the 150 GHz data—over 150 GHz data alone. We find very little further improvement when we add the 220 GHz data, which has a factor of five higher noise than the 150 GHz data. As the 220 GHz SPT maps are not currently deep enough to add significantly to the cluster detection efficiency, we use only 95 and 150 GHz data for all the results presented in this work.

For one field, ra5h30dec-55, only 150 and 220 GHz data exist, and we only perform single-frequency 150 GHz cluster finding on this field’s map (with results indistinguishable from those reported in V10). Using the measured improvement in cluster S/N in multi-band vs. single-band data (roughly 20% averaged across all redshifts and cluster sizes), we determined that the most significant cluster in this field would not have made it into the catalog in this work even if we had 95 GHz data on this field (see Section 3 for details of the selection of clusters for this work).

3. CATALOG

The cluster-finding pipeline described above returns hundreds or even thousands of candidates (depending on the threshold value of ξ) within the 2500 deg^2 survey area. Some of these candidates have already been reported in S09 and V10, and upcoming publications will continue to expand the SPT catalog, including candidates down to S/N values as low as $\xi = 4.5$, where the purity of the sample is still estimated to be well over 50%. The aim for this paper, however, is to search the full survey area for the clusters that have the greatest potential to test the current cosmological model—in other words, the most massive clusters. At any given redshift, the most massive clusters will correspond to the clusters with the highest SZ significance, so we present here a catalog of the 26 most significant detections in the 2500 deg^2 survey area.

This catalog is constructed by setting a high significance threshold of $\xi \geq 7$ for all shallow fields. This threshold was chosen to ensure zero false detections at high confidence (see Section 4 for details on the false detection rate estimate) and to limit the scattering of low-mass systems into the sample. To choose a deep-field threshold to match this shallow-field threshold, we

use simulated observations (described in Section 4) at both field depths using the same underlying simulated SZ skies. For each cluster which met the $\xi \geq 7$ threshold in the shallow-field simulations, a deep-field ξ was calculated. The shallow-to-deep ξ ratio was then calculated for each cluster and found to vary from 0.4–0.6, depending on cluster characteristics. These ratios were averaged to yield an approximately equivalent threshold value of $\xi \geq 13$ for the full-depth fields. Note, however, that significance values do not scale simply with field depth. The matched-filter noise is a combination of the CMB, point sources and observational noise, and the relative contribution of each is k -dependent, varying significantly between the different depths. For example, in shallow fields the relative contribution of the CMB is less, tilting the matched filter to prefer larger scales; correspondingly, it prefers smaller scales in deep fields. A simple, direct translation of “preview-depth ξ ” to “full-depth ξ ” is therefore not possible on a cluster-by-cluster basis; the matching of thresholds is approximate and designed only to match the average scaling.

Nevertheless, as shown in Figure 2, the rough 50% and 90% completeness contours using the two depths are fairly well matched, particularly at high redshift. These contours are calculated as in V10, by matching detections in simulated observations with halos identified in the underlying dark matter simulations in bins of mass and redshift. For the high ξ thresholds in this work—which correspond to very massive dark matter halos—the number of matching halos is small in most bins, so the completeness contours are poorly sampled and noisy, but the general agreement between the two sets of contours is clear. Note that the uncertainty in these curves does not directly affect the remainder of this work, as the selection function is always considered as a strict threshold in ξ ; the selection as a function of mass and redshift is presented in Figure 2 purely for illustrative purposes.

For each cluster, both the redshift, and the X-ray luminosity were determined (as outlined in Section 5 and Section 6). The catalog is presented in Table 6 and thumbnail images of each cluster in the SZ and optical/IR are shown in Appendix A.

3.1. Notable Clusters

Of the 26 clusters reported in this paper, 12 are new discoveries, one was previously reported in V10, and 13 others have been identified in other optical, X-ray, and SZ cluster catalogs, with 7 having multiple identifications. The previously identified clusters include seven clusters in the optical Abell catalog (Abell et al. 1989), nine clusters in the X-ray ROSAT-ESO Flux Limited X-ray Galaxy cluster survey catalog (REFLEX, Böhringer et al. 2004a), and six clusters in the mm-wave Atacama Cosmology Telescope catalog (ACT, Marriage et al. 2011). These cross-associations and alternative identifications are noted in Table 6. In this section, we discuss particularly notable clusters in the SPT catalog.

SPT-CL J0102-4915— This cluster was first reported in Marriage et al. (2011). It is the most significant detection to date in the full SPT survey by nearly a factor of two. It has a comparable X-ray luminosity and beam-averaged SZ decrement to the Bullet cluster and AS1063, whose SZ significances should be similar when the SPT survey

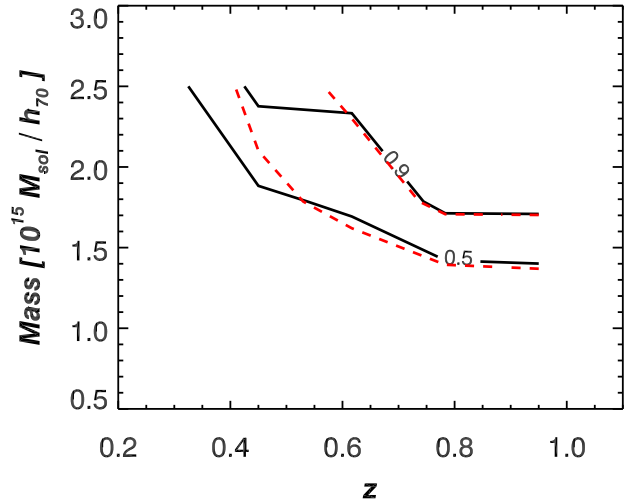


FIG. 2.— Completeness contours as a function of mass ($M_{200}(\rho_{\text{mean}})$) and redshift for both sets of map depths and ξ thresholds, estimated from simulated observations. 50% and 90% contours are shown for shallow fields with $\xi \geq 7$ (black, solid lines) and for deep fields with $\xi \geq 13$ (red, dashed lines).

is completed to full depth. Given the redshift of this cluster ($z = 0.78$), it is expected to be one of the rarest objects in the SPT survey (see Figure 5).

SPT-CL J0615-5746— This cluster has the second highest redshift of any cluster in this paper, with a redshift of $z = 0.972$. Based on its ROSAT faint source catalog counterpart, it is measured to be the fourth most X-ray luminous cluster in this catalog (see Section 6).

SPT-CL J0658-5556— This cluster is the well-known Bullet cluster, otherwise known as 1ES 0657-558. It has been extensively studied in multiple wavelengths (e.g., Clowe et al. 2006) and is known to be one of the most massive and X-ray-luminous clusters in the Universe. It is expected to be the most massive cluster in the final SPT catalog.

SPT-CL J2106-5844— Multi-wavelength observations of this SPT-discovered cluster are discussed in detail in Foley et al. (2011). This is the highest-redshift cluster ($z = 1.132$) spectroscopically confirmed in the SPT survey. X-ray observations from *Chandra* measure an X-ray luminosity of $L_X[0.5-2.0 \text{ keV}] = 13.9 \times 10^{44} \text{ erg s}^{-1}$ (Foley et al. 2011), comparable to the X-ray luminosity of the Bullet cluster. The mass we report in Table 6 for SPT-CL J2106-5844 is slightly (5–10%) discrepant with the SZ mass reported in Foley et al. (2011), although the difference is much smaller than either value’s 1σ uncertainty. The difference arises because Foley et al. (2011) use the single-band 150 GHz ξ and the exact V10 scaling relation to derive the mass, whereas this work uses the multi-band ξ and the multi-band scaling relation developed specifically for this work. (See Section 4.1 and V10 for details on the mass estimation and scaling relations.)

SPT-CL J2248-4431— This cluster is also known as AS1063. It is the second most X-ray luminous cluster in the REFLEX X-ray survey (Böhringer et al. 2004a), even more luminous than the Bullet cluster. It has the

second highest estimated mass for any cluster in this paper.

SPT-CL J2344-4243— From its redshift and its ROSAT bright source catalog counterpart (see Section 6), this cluster is measured to have the largest X-ray luminosity of any cluster in this paper. A bright Type 2 Seyfert galaxy at redshift 0.5975, 2MASX J23444387-4243124, is located 19'' from the SZ cluster centroid. This redshift is consistent with our photometric red-sequence redshift estimate of 0.62 for the cluster (see Section 5), suggesting this galaxy may be in or near this cluster.

3.2. Point Source Veto

As discussed in Section 2.4, emissive sources above 5σ are masked in the cluster finding procedure, and any cluster detections within 8' of a masked point source are rejected, because residual source flux or artifacts due to the masking can cause spurious decrements when the maps are filtered. However, this rather conservative procedure can result in rejecting a cluster detection that was only marginally affected by the nearby emissive source.

To test this scenario, we re-ran the cluster finding algorithm on all the fields used in this work with only the very brightest ($S_{150\text{GHz}} > 50 \text{ mJy}$) sources masked (as compared to the 5σ thresholds of roughly 6.4 and 17 mJy in the full-depth and shallow fields). Each detection above the ξ threshold for this paper was visually inspected, and the vast majority were rejected as obvious point-source-related artifacts. However, two objects were clearly real detections. One of these detections, with $\xi = 19.3$ (in a full-depth field), is a known cluster (Abell S0295), and we include it in our catalog as SPT-CL J0245-5302. There are two $> 5\sigma$ sources within 8 arcmin of this cluster, but neither is strong enough to affect the ξ measurement by more than 1 or 2σ . Furthermore, the sources lie to the north and south of the cluster, and wings from the matched filter are predominantly along the scan direction (east-west in all SPT fields but one). However, because this cluster was not found by the original version of the cluster finding algorithm, we do not include it any cosmological analysis.

The other detection, $\xi = 13.3$ (full-depth), has an 8 σ source almost directly to the east. Because this cluster (SPT-CL J2142-6419, which will likely appear in a future catalog) could have been bumped over our $\xi = 13$ full-depth threshold by the filtering wing of the point source, we choose not to include it in this work.

4. SIMULATIONS

Simulated observations were used to characterize the catalog presented in this work. These simulations were modeled after those used in V10, where full details can be found; a brief summary is provided here.

We create random Gaussian realizations of the power spectra of primary CMB anisotropy, kSZ, and point sources below the SPT detection threshold. The primary CMB power spectrum is chosen to match the WMAP7 best-fit Λ CDM model (Larson et al. 2011), and we add the Sehgal et al. (2010a) predicted kSZ power spectrum to the expected CMB anisotropy. The point-source power spectrum includes terms corresponding to synchrotron-dominated sources and DSFGs with amplitudes based on the results of Shirokoff et al. (2011). We

include Gaussian realizations of the power from Poisson distributions of both sources with amplitudes at 150 GHz and $k = 3000$ of $D_{3000}^r = 1.3 \mu\text{K}^2$ for the synchrotron sources and $D_{3000}^{\text{dsfg}} = 7.7 \mu\text{K}^2$ for the DSFGs. We assume a spectral index of $\alpha = -0.6$ for the synchrotron sources and $\alpha = 3.6$ for DSFGs. In addition to the Poisson power, we model a clustered DSFG component with an angular multipole dependence of $D_k \propto k$ and amplitude at 150 GHz and $k = 3000$ of $D_{3000}^c = 5.9 \mu\text{K}^2$. SZ skies were simulated as in V10 using the methodology of Shaw et al. (2009); the fiducial simulations from that work are used here. Briefly, they consist of semi-analytic gas models pasted over halos identified in N-body dark matter simulations. At each frequency (95 and 150 GHz), forty 100 deg² sky maps were generated.

These simulated skies were processed with an analytic approximation to the SPT transfer function, consisting of a Gaussian beam, an isotropic high-pass filter and a high-pass filter along the R.A. direction. The filters were arranged to model the effect of the SPT data processing described in Section 2.3, with the R.A. high-pass set to match the $k_{\text{R.A.}} = 400$ cutoff of the Fourier mode removal and the isotropic high-pass set at $k = 500$ to approximate the spatial template removal.

Noise realizations were generated at each frequency for both the full survey and preview depths. The noise power was measured in differenced (jackknife) maps for each field, and these powers were averaged across the set of fields at each frequency and depth. Forty Gaussian random realizations of each of these averages were then generated and added to the processed simulated sky maps.

These simulations were then subjected to the same cluster-finding pipeline applied to the real data, and recovered clusters were matched with the underlying catalog of massive halos associated with the SZ simulations.

4.1. Mass Scaling Relations and Unbiased Mass Estimates

A number of different techniques are available for obtaining cluster mass estimates from SZ measurements. The integrated SZ flux, Y , is expected to be a tight proxy for the cluster mass (Barbosa et al. 1996; Holder & Carlstrom 2001; Motl et al. 2005; Nagai et al. 2007; Shaw et al. 2008; Staneck et al. 2009). Unfortunately, the difficulty in determining the correct filter scale θ_c from SPT data alone adds significant scatter to the scaling relation of mass with Y (see V10 for details).³⁷ In simulations, the SPT significance ξ has a smaller scatter than our current integrated Y estimates, and, as in V10, we use the significance as a mass proxy.

Due to the significant impact of noise biases, a direct ξ - M scaling relation is complex and difficult to characterize. Instead, following the prescription of V10, we introduce an unbiased significance ζ , whose scaling with mass $M_{200}(\rho_{\text{mean}})$ takes the form

$$\zeta = A \left(\frac{M}{5 \times 10^{14} M_{\odot} h^{-1}} \right)^B \left(\frac{1+z}{1.6} \right)^C, \quad (6)$$

where A is a normalization, B a mass evolution and C a

³⁷ Effort is currently underway to use our multi-frequency data to improve the determination of θ_c .

TABLE 2
MASS SCALING RELATIONS

| Depth | A | B | C | Scatter |
|-------------|------|------|------|---------|
| Full survey | 7.50 | 1.32 | 1.64 | 0.21 |
| Preview | 3.50 | 1.29 | 0.87 | 0.16 |

redshift evolution.³⁸ In simulated maps of both depths, ζ was calculated for each cluster as in V10, by determining the preferred filter scale and cluster position in the absence of noise then averaging the detection significance at that filter scale and position over many noise realizations. Mass scaling relations were fit to the subset of these with $M > 2 \times 10^{14} h^{-1} M_{\odot}$ and $z > 0.3$ by minimizing the residual logarithmic scatter in ζ about the relation.³⁹ These relations are given in Table 2. As these are based on the same SZ simulations used in V10, they can be viewed as equivalent to the relations presented in that work.

Uncertainties in the SZ modeling lead to significant systematic uncertainties on these scaling relation parameters. Following V10, we apply conservative 30%, 20%, 50%, 20% Gaussian uncertainties to A, B, C, and scatter, respectively.

Mass estimates are constructed as in V10 with slight modifications to account for the different field depths. Details of the conversion from ξ to mass are given in Appendices B and D of V10. Briefly, we calculate the conditional probability of detecting a cluster of mass M at a given value of ξ , $P(\xi|M)$, and then apply a mass-function prior to create the posterior probability $P(M|\xi)$. This procedure accounts for two types of bias in the mass estimate, the first due to the fact that we have maximized ξ over many filter choices and positions in the map, and the second due to the combination of the steepness of the cluster mass function and observational noise or scatter in the mass-observable scaling-relation. The latter effect, which results in more low-mass systems scattering up into a given ξ bin than high-mass systems scattering down, is related to the phenomenon of Eddington bias⁴⁰ (Eddington 1913). For the very high detection significances used in this work, the maximization bias is completely negligible compared to the bias due to this asymmetric scatter. As in V10, we use the Tinker et al. (2008) mass function evaluated at the maximum likelihood point in the WMAP7+V10 chain as our prior. This method produces unbiased posterior estimates for cluster masses, assuming the validity of the simulations and of the various priors applied.

In Andersson et al. (2010), we compared SZ inferred masses calculated with this method to X-ray mass estimates for the 15 clusters from V10 that had X-ray measurements. Overall, we found agreement between the SZ and X-ray mass estimates near the quoted level of the

³⁸ Note that, for consistency with V10, this relation is given in terms of h (i.e., h_{100}), not h_{70} .

³⁹ The redshift cutoff is due to the fact that it was found in V10 that the power-law parametrization of the scaling relation fails to fully capture the behavior of the SPT selection function below $z = 0.3$.

⁴⁰ Strictly speaking, “Eddington bias” refers to the bias in number counts caused by this asymmetric scatter. The bias in the measured properties of individual objects is sometimes erroneously referred to as “Malmquist bias”.

systematic uncertainties of the SZ mass estimates. However, there was a significant statistical offset, with the SZ-inferred masses lower by a factor of 0.78 ± 0.06 averaged over the sample, which we do not correct for in the masses in Table 6. This factor could have a redshift or mass dependence and naively applying a correction factor would ignore these effects. There was some evidence for this in Andersson et al. (2010), where the lowest redshift and most massive cluster had the most discrepant SZ and X-ray inferred masses. We are currently pursuing an analysis that jointly constrains the SZ and X-ray mass-observable relations with cosmology (Benson et al. 2011), which will more accurately quantify any systematic offset between the SZ and X-ray mass estimates. For this work, we consider the quoted uncertainty of the SZ mass estimates to be a reasonable estimate of the systematic uncertainty, and note that there is some evidence that the SZ mass estimates are low by $\sim 25\%$. We show in Section 7 that none of the conclusions in our cosmological analyses would change if we naively applied this scaling factor.

Finally, we note that, although the scaling relation fits were only performed on simulated clusters above $z = 0.3$, we nevertheless report SZ-derived masses for several $z < 0.3$ clusters in Table 6. These mass estimates are extrapolations of the scaling relations to areas of parameter space in which they have not been tied to simulations and may therefore be subject to further systematic uncertainties. For this reason, we do not use any clusters at $z < 0.3$ in the likelihood calculations described in Section 7.2.

4.2. Purity and Completeness

To test the likelihood of false detections, simulated observations were generated omitting the SZ signal, and run through the cluster-finding pipeline. The false detection rate was found to be a rapidly falling function of the detection threshold. No false detections were found above a significance of $\xi = 6$ in simulations of 4000 deg^2 at either depth. Given that the lowest threshold used in generating the catalog presented in this work is $\xi \geq 7$, it is highly improbable that it contains any false detections. This is confirmed by the multi-band followup, which shows counterparts for each cluster in the catalog.

The catalog is complete above threshold ξ values by construction. As discussed in Section 3, two factors make it difficult to quantitatively convert this into a mass and redshift completeness. The clusters in this catalog lie at the extreme high-mass end, and, as such, are rare in the simulated skies, yielding insufficient statistics to obtain a robust estimate of their detectability. Furthermore, there is large uncertainty associated with modeling the gas attached to halos in the simulation that makes any threshold uncertain at the $\sim 30\%$ level. Figure 2 shows our best estimate of 50% and 90% completeness for the two sets of field depths and ξ thresholds. We note that, as the same simulated SZ skies were used for both depths, the variance due to the limited sample size will appear as a coherent shift, rather than a scatter, between the two sets of curves.

5. OPTICAL AND INFRARED DATA

Multi-band imaging from both ground- and space-based facilities has been obtained for clusters in the cat-

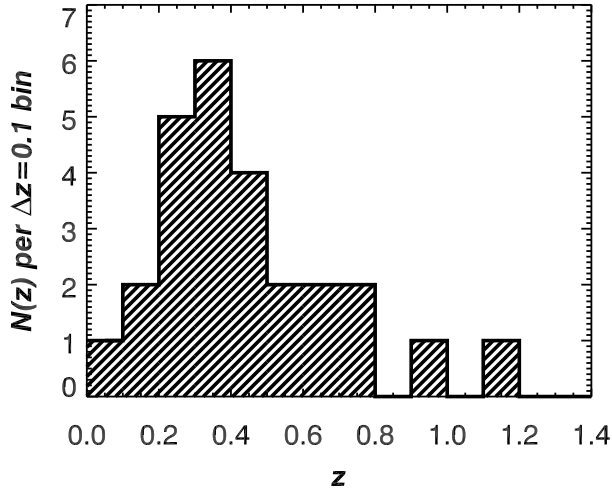


FIG. 3.— Redshift histogram of the sample.

alog, for the purpose of cluster redshift estimation where no previous spectroscopic redshift could be determined from the literature. We have also carried out new multi-slit spectroscopy on some of the clusters. A summary of the cluster redshifts is shown in Table 3, and a description of our methods is outlined below. Figure 3 shows the redshift histogram of our cluster sample.

5.1. Ground-based Imaging

The previously unknown clusters in this catalog were imaged with the cameras shown in Table 4. The Swope 1 m at Las Campanas Observatory, equipped with the SITE3 CCD detector and *BVRI* filters, provided sensitivity to clusters at $z \lesssim 0.7$. We chose at least two passbands that spanned the 4000 Å break, as determined initially using cluster redshifts estimated by eye from Digitized Sky Survey (DSS) images. We required a detection of $0.4L^*$ early-type cluster galaxies at about 5σ . We then iterated on this strategy: if the cluster was still not sufficiently detected in the initial set of exposures, we updated our best redshift estimate using the new data, if possible, and reobserved.

The Blanco 4 m at Cerro Tololo Inter-American Observatory and the Magellan 6.5 m telescopes at Las Campanas Observatory, provided sensitivity to clusters at $z \lesssim 1$. The Blanco/MOSAIC-II, Magellan/LDSS3, and Magellan/IMACS CCD cameras were used with *griz* filters. The same iterative strategy was implemented until we reached our required detection.

As detailed in Foley et al. (2011), 50 min of preimaging with the VLT’s FORS2 camera in *I* provided additional broadband data for our highest-redshift cluster, SPT-CL J2106-5844, in our corresponding spectroscopic program.

All images were reduced in a uniform manner using the same software and methods described in detail in the previous, closely related work of High et al. (2010, hereafter H10). Photometry was calibrated using the Stellar Locus Regression method (High et al. 2009). The red-sequence redshifts reported in Table 3 were derived using

the same red-sequence software described in H10. These redshifts are estimated to be accurate to $\sigma_z/(1+z) \approx 2\text{--}3\%$ (statistical plus systematic), as determined using a larger subset of clusters with added spectroscopic redshift data. An exception to this are the SWOPE derived redshifts (SPT-CL J0245-5302 and SPT-CL J0411-4819) which are accurate to $\sigma_z/(1+z) \approx 4\text{--}5\%$. This was due to using Johnson filters (as opposed to Gunn-Sloan filters), and calibrating the photometry with a synthetic stellar locus (rather than the median SDSS stellar locus from Covey et al. (2007)) using the PHOENIX stellar model atmosphere library (Brott & Hauschildt 2005).

A parallel reduction of the Blanco/MOSAIC-II data was performed using the Dark Energy Survey data management system (Ngeow et al. 2006; Mohr et al. 2008). Redshifts for the 12 clusters with MOSAIC-II imaging were independently measured from these data using Artificial Neural Network (ANNz Collister & Lahav 2004) software and another red-sequence method (Song et al, in prep). This independent cross-checking led to consistent redshift estimates in all cases, except for SPT-CL J0615-5746, where redshift estimates ranged from about 0.9 to 1.1 (this cluster was later spectroscopically confirmed at $z = 0.972$); and SPT-CL J0555-6405, where different estimates gave redshifts of 0.27, 0.35, and 0.42. In the latter case, because the red sequence appears most pronounced and unambiguous at 0.42, we report the redshift from the H10 software only.

An additional cross-check for two of the clusters presented here is provided by Menanteau et al. (2010), who estimated photometric redshifts of 0.75 ± 0.04 for SPT-CL J0102-4915 (compare our result of 0.78), and 0.54 ± 0.05 for SPT-CL J0438-5419 (compare 0.45).

5.2. Spitzer Space Telescope Imaging

Spitzer/IRAC imaging is particularly important for the confirmation and study of high-redshift SPT clusters, such as SPT-CL J2106-5844 at $z = 1.132$ (Figure 26), where the optically faint members are strongly detected in the mid-infrared. Three of our catalog clusters were observed as part of a larger program to follow up clusters identified in the SPT survey. The on-target observations consisted of 8×100 s and 6×30 s dithered exposures at 3.6 and 4.5 μ m, respectively. The deep 3.6 μ m observations are sensitive to passively evolving cluster galaxies down to $0.1 L^*$ at $z = 1.5$. The data were reduced exactly as in Brodwin et al. (2010), following the method of Ashby et al. (2009). Briefly, we correct for column pull-down and residual image effects, mosaic the individual exposures, resample to 0''.86 pixels (half the solid angle of the native IRAC pixels), and reject cosmic rays.

5.3. Spectroscopy

Eleven of the clusters in this work have published spectroscopic redshifts, which we note in Table 3. Using the instruments listed in Table 5, we present new spectroscopic redshift measurements on five clusters, four of which have no such previously published data. The robust biweight location estimator is used to determine the cluster spectroscopic redshifts from ensembles of member galaxies.

5.3.1. SPT-CL J0234-5831 and SPT-CL J0254-5857

TABLE 3
CLUSTER REDSHIFT DATA

| Object Name | z_{spec} | Spectroscopy Ref. ^a | # members | z_{rs} | Imaging Ref. ^b |
|-------------------|-------------------|--------------------------------|-----------|-----------------|---------------------------|
| SPT-CL J0040-4407 | ... | ... | ... | 0.40 | im1 |
| SPT-CL J0102-4915 | ... | ... | ... | 0.78 | im1 |
| SPT-CL J0232-4421 | 0.284 | de Grandi et al. (1999) | ... | ... | ... |
| SPT-CL J0234-5831 | 0.415 | sp2 | 21 | 0.44 | im3, im4 |
| SPT-CL J0243-4833 | ... | ... | ... | 0.53 | im1, im4 |
| SPT-CL J0245-5302 | 0.300 | Edge et al. (1994) | ... | 0.35 | im4 |
| SPT-CL J0254-5856 | 0.438 | sp2 | 32 | 0.43 | im3, im4 |
| SPT-CL J0304-4401 | ... | ... | ... | 0.52 | im1 |
| SPT-CL J0411-4819 | ... | ... | ... | 0.42 | im4 |
| SPT-CL J0417-4748 | ... | ... | ... | 0.62 | im1, im7 |
| SPT-CL J0438-5419 | ... | ... | ... | 0.45 | im1, im4 |
| SPT-CL J0549-6204 | ... | ... | ... | 0.32 | im1 |
| SPT-CL J0555-6405 | ... | ... | ... | 0.42 | im1 |
| SPT-CL J0615-5746 | 0.972 | sp3 | 1 | 1.0 | im1, im6 |
| SPT-CL J0628-4143 | 0.176 | de Grandi et al. (1999) | ... | 0.21 | im1 |
| SPT-CL J0638-5358 | 0.222 | de Grandi et al. (1999) | ... | ... | ... |
| SPT-CL J0645-5413 | 0.167 | de Grandi et al. (1999) | ... | ... | ... |
| SPT-CL J0658-5556 | 0.296 | Tucker et al. (1998) | ... | ... | ... |
| SPT-CL J2023-5535 | 0.232 | Böhringer et al. (2004b) | ... | 0.23 | im2, im3, im4 |
| SPT-CL J2031-4037 | 0.342 | Böhringer et al. (2004b) | ... | ... | ... |
| SPT-CL J2106-5844 | 1.132 | sp4, see Foley et al. (2011) | 18 | 1.17 | im5, im6, im7 |
| SPT-CL J2201-5956 | 0.098 | Struble & Rood (1999) | ... | ... | im2, im6 |
| SPT-CL J2248-4431 | 0.348 | Böhringer et al. (2004b) | ... | ... | ... |
| SPT-CL J2325-4111 | ... | ... | ... | 0.37 | im1 |
| SPT-CL J2337-5942 | 0.776 | sp5; also sp1, see H10 | 20 | 0.77 | im2, see H10; im7 |
| SPT-CL J2344-4243 | ... | ... | ... | 0.62 | im1 |

NOTE. — Spectroscopic and red-sequence redshift information for the cluster sample.

^a Cross-reference to spectroscopic redshift data from external and internal sources. Internal references are denoted “sp#” and refer to Table 5.

^b Cross-reference to broadband redshift data from external and internal sources. Internal references are denoted “im#” and refer to Table 4.

TABLE 4
OPTICAL AND INFRARED IMAGERS

| Alias ^a | Site | Telescope | Aperture (m) | Camera | Filters ^b | Field | Pixel scale (") |
|--------------------|--------------|-------------------------|--------------|-----------|-----------------------|--------------------|-----------------|
| im1 | Cerro Tololo | Blanco | 4 | MOSAIC-II | <i>griz</i> | $36' \times 36'$ | 0.27 |
| im2 | Las Campanas | Magellan/Baade | 6.5 | IMACS f/2 | <i>griz</i> | $27'4 \times 27'4$ | 0.200 |
| im3 | Las Campanas | Magellan/Clay | 6.5 | LDSS3 | <i>griz</i> | 8/3 diam. circle | 0.189 |
| im4 | Las Campanas | Swope | 1 | SITe3 | <i>BVRI</i> | $14'8 \times 22'8$ | 0.435 |
| im5 | Paranal | VLT | 8.2 | FORS2 | <i>I</i> | $6'8 \times 6'8$ | 0.25 |
| im6 | Cerro Tololo | Blanco | 4 | NEWFIRM | <i>JK_s</i> | $28' \times 28'$ | 0.4 |
| im7 | ... | Spitzer Space Telescope | 0.85 | IRAC | [3.6][4.5] | $5'2 \times 5'2$ | 1.2 |

NOTE. — The optical and infrared cameras used. The choice of facilities and filters for any given cluster was typically optimized according to our best redshift estimate prior to observation. Not all imagers, nor all the listed filters, were used on each cluster.

^a Shorthand alias used in Table 3.

^b The filters we used, which were in general a subset of all of those available. We did not typically use all listed filters on each cluster.

TABLE 5
OPTICAL AND INFRARED SPECTROGRAPHS

| Alias ^a | Site | Telescope | Aperture (m) | Camera | Mode |
|--------------------|--------------|----------------|--------------|--------|----------|
| sp1 | Las Campanas | Magellan/Clay | 6.5 | LDSS3 | longslit |
| sp2 | Las Campanas | Magellan/Baade | 6.5 | IMACS | GISMO |
| sp3 | Las Campanas | Magellan/Baade | 6.5 | IMACS | longslit |
| sp4 | Paranal | VLT | 8.2 | FORS2 | MOS |
| sp5 | Cerro Pachon | Gemini South | 8.1 | GMOS | MOS |

NOTE. — The spectrographs used.

^a Shorthand alias used in Table 3.

In a procedure similar to Brodwin et al. (2010), multi-slit spectroscopic observations were acquired on the 6.5-meter Baade Magellan telescope on UT 2010 October 8 for SPT-CL J0234-5831 and SPT-CL J0254-5857. Measurements were made using the Gladders Image-Slicing Multislit Option (GISMO, Gladders et al. in prep.) module on the Magellan/IMACS spectrograph. GISMO optically remaps the central region of the IMACS field of view (roughly $3.5' \times 3.2'$) to sixteen evenly-spaced regions of the focal plane, allowing for a large density of slitlets in the cluster core while minimizing trace overlaps on the CCD.

In designing the multislit mask, galaxies were assigned a weight proportional to their r-band brightness and adjusted for their position in color space with respect to a manually-selected red sequence. The f/4 camera, the 300 l/mm grating and the $z1430 - 675$ filter were used. Each cluster was observed with three 30-min exposures of one mask in good seeing ($\sim 0.6''$).

The COSMOS reduction package was used for standard CCD processing, resulting in wavelength-calibrated 2D spectra. The 1D spectra were then extracted from the sum of the reduced data. Secure redshifts were obtained for 21 member galaxies of SPT-CL J0234-5831, and 32 member galaxies of SPT-CL J0254-5857.

5.3.2. SPT-CL J0615-5746

Longslit spectroscopy of SPT-CL J0615-5746 was performed on UT 2011 March 8, also with the IMACS spectrograph on the Baade Magellan telescope. The longslit was aligned across several objects and yielded clear redshifts for the BCG and a second cluster member. The reported redshift is that of the BCG.

5.3.3. SPT-CL J2106-5844

We refer the reader to Foley et al. (2011) for a detailed description of spectroscopic measurements of SPT-CL J2106-5844. In short, the redshift given in Table 3 is derived from 18 member galaxies using VLT/FORS2 and Magellan/IMACS-GISMO.

5.3.4. SPT-CL J2337-5942

The redshift of SPT-CL J2337-5942 reported in Table 6, $z_{\text{spec}} = 0.776$, is from combined measurements of 19 cluster members using GMOS on the 8.1 m Gemini South telescope and 2 members using the Magellan/LDSS3 longslit—one of which overlaps with a GMOS member—for a total of 20 cluster members. The LDSS3 data were described in detail in H10, where $z_{\text{spec}} = 0.781$ was reported from the two members.

For the new GMOS observations we are presenting here, galaxies with $r - i$ color consistent with a cluster red-sequence at $z = 0.77$, and having non-stellar PSFs in the Gemini i -band pre-image, were used to populate two masks. A total of 31 galaxies were observed for three hours with the R150-G5326 grism and the GG455-G0329 filter. The IRAF Gemini reduction package was used for standard CCD processing. The wavelength-calibrated 2D spectra were sky-subtracted using an in-house routine, after which the 1D spectra were extracted from the coadded 2D spectra. Secure redshifts for the 19 cluster members were obtained from the GMOS masks. All the spectra are from early-type galaxies, often exhibiting a very strong Ca H&K absorption feature.

6. X-RAY DATA

For each cluster in Table 6, we searched the ROSAT data archive for possible X-ray counterparts, including the REFLEX catalog (Böhringer et al. 2004a), the ROSAT All-Sky Survey Bright Source Catalog (Voges et al. 1999), and the ROSAT All-Sky Survey Faint Source Catalog⁴¹. We also used data from the ROSAT All Sky Survey and pointed Position Sensitive Proportional Counter (PSPC) observations to measure the X-ray flux for the SPT clusters in the “hard” 0.6-2 keV energy band, since the signal to noise is generally better in this band than in the full ROSAT energy range (Vikhlinin et al. 1998). To determine the source counts, we used a source radius corresponding to 2 Mpc, excluded any sources not associated with the cluster emission and used a nearby region for measuring the X-ray background. Significant detections were found for 25 of the 26 clusters in the ROSAT observations. The highest-redshift cluster, SPT-CL J2106-5844, was not detected by ROSAT, but has been detected in pointed observations with *Chandra* (Foley et al. 2011).

To determine the cluster flux and luminosity, we used PIMMS⁴² to determine the cluster unabsorbed flux in the observer’s frame from the ROSAT “hard” band observations. We then used the XSPEC⁴³ “flux” and “lumin” functions to determine the cluster luminosity in the cluster rest frame, which we report in Table 6. We report each in the 0.5-2.0 keV band because of this band’s relative insensitivity to the assumed X-ray temperature. For example, the inferred flux changes by $\lesssim 2\%$ when assuming a range of gas temperatures between 6 to 10 keV. For two clusters, SPT-CL J2106-5944 and SPT-CL J2337-5942, we give the flux and luminosity measured by *Chandra* and reported in Foley et al. (2011) and Andersson et al. (2010), respectively.

In Figure 4, we plot the X-ray luminosity, L_X , and the SPT measured mass (converted from $M_{200}(\rho_{\text{mean}})$ to $M_{500}(\rho_{\text{crit}})$) from Table 6. We plot only statistical uncertainties for both luminosity and mass. However, we note that we have ignored several important systematic uncertainties in the ROSAT X-ray luminosity measurements, including the effects of unresolved point sources and cooling cores. These can add biases and additional scatter to the X-ray measurements, however cannot observationally be accounted for because of the relatively large ROSAT beamsize. Similar phenomena also affect the SZ measurements, however they are accounted for statistically in the significance estimate and the scatter in the significance-mass relation, as described in Section 4.1. The latter dominates the statistical uncertainty of the SZ mass estimates. In Figure 4, we have assumed the best-fit redshift evolution in the $L_X - M$ relation measured by Vikhlinin et al. (2009a), where $L_X \propto ME(z)^{1.85}$. This is slightly different than the self-similar expectation that predicts an evolution of $E(z)^2$ for the luminosity in the 0.5-2.0 keV band and an evolution of $\sim E(z)^{7/3}$ for the bolometric luminosity, which has an additional weak dependence of luminosity with temperature.

In Figure 4, we also show the best-fit $L_X - M$ rela-

⁴¹ <http://heasarc.gsfc.nasa.gov/W3Browse/rosat/rassfsc.html>

⁴² <http://cxc.harvard.edu/toolkit/pimms.jsp>

⁴³ <http://heasarc.nasa.gov/xanadu/xspec/xspec11/index.html>

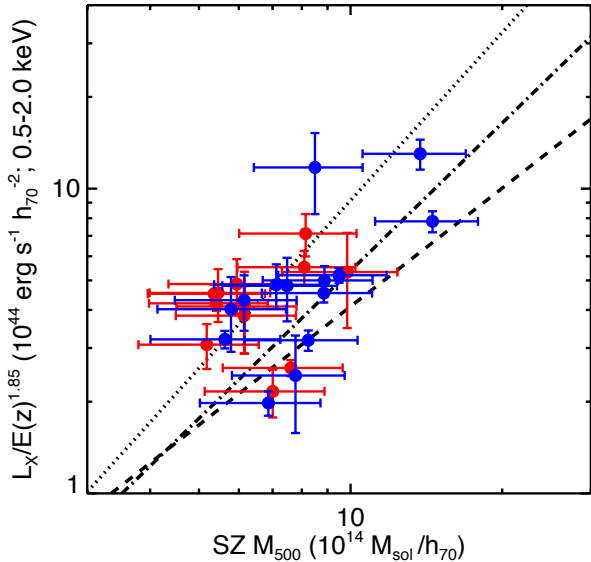


FIG. 4.— The X-ray luminosity and SZ inferred masses $M_{500}(\rho_{\text{crit}})$ for our cluster sample. We plot statistical uncertainties only, and note that the statistical uncertainty of the SZ mass estimate is limited by the assumed scatter in the SZ significance-mass relation. Clusters from the shallow fields are in blue, and clusters from the deep fields are in red. We also show the best-fit relations of Pratt et al. (2009) (dotted), Vikhlinin et al. (2009a) (dash-dot), and Mantz et al. (2010) (dashed).

tions from Pratt et al. (2009), Vikhlinin et al. (2009a), and Mantz et al. (2010), to compare our results with other X-ray cluster studies. Both Pratt et al. (2009) and Mantz et al. (2010) assume evolution consistent with the self-similar relation for bolometric luminosity. For each result, we use their published normalization and slope, but have assumed the redshift evolution measured by Vikhlinin et al. (2009a). Relative to self-similar evolution, this would cause a < 7% change in the normalization for the typical redshift range of their cluster samples ($z < 0.3$). Mantz et al. (2010) also quote their luminosities in the rest frame 0.1-2.4 keV band, which we have converted to 0.5-2.0 keV by dividing by a factor of 1.61. This factor is appropriate for a cluster with a 8 keV electron temperature, and varies negligibly with temperature. We expect that both approximations will not significantly change the normalization of either relation. As can be seen in Figure 4, there is a fairly large spread in the published L_X - M relations, although the methods and samples differ between each work. For example, they each use cluster samples with somewhat different mass and redshift ranges, and account for the effects of Eddington bias differently. Regardless, we consider the agreement with other cluster samples reasonable, and also significant given the unique SZ selection of the clusters in this work. The X-ray selected cluster samples are of generally lower redshift, less massive, and have been corrected for Malmquist bias from the X-ray flux selection, a bias that is completely absent for SZ selected samples. This work confirms that the SPT cluster sample consists of very massive clusters, which qualitatively follow the L_X - M relation measured from other X-ray selected cluster samples.

7. DISCUSSION

The 26 highest-significance SZ-selected clusters from the 2500 deg^2 SPT survey (see Table 6) include all the most massive galaxy clusters in this region of the sky, independent of the cluster redshift. These exceedingly rare systems populate the high end of the mass function at each redshift, and predictions for the characteristics of this population are sensitive to the details of the assumed cosmological model. An interesting first step in using the clusters presented in this work to constrain cosmology is to ask whether their distribution in mass and redshift is consistent with the predictions of the standard Λ CDM cosmological model. We investigate this question two ways. First, we use the framework of Mortonson et al. (2011, hereafter M11) and the fitting functions they provide to ask whether the existence of any single cluster in our sample is in significant tension with Λ CDM. We then fit all available cosmological data including this new cluster sample to two different cosmological models—namely, standard Λ CDM and a single-parameter extension allowing for non-Gaussian initial conditions—and see if the data prefer the non-standard model.

7.1. Single-cluster Tests

M11 have published fitting functions that allow us to answer the question: Is this one cluster in significant tension with Λ CDM? In Figure 5, we plot the mass vs. redshift for all 26 clusters and overplot exclusion curves from M11. As explained in Appendix C of M11, the mass for a given cluster that is appropriate to compare to their exclusion curves is not precisely the best posterior estimate of that cluster's mass. The masses plotted in Figure 5 are calculated using Equation C3 from M11, using the conditional probability $P(\xi|M)$ to estimate their M_{obs} and $\sigma_{\ln M}$ and using the local slope of the Tinker et al. (2008) mass function around the value of M_{obs} for γ . The error bars on the masses in Figure 5 are calculated by setting the fractional error (i.e., the error in $\ln M$) equal to the fractional error of the posterior mass estimates in Table 6. We have confirmed that this is an excellent approximation to the full probability distribution of the M11-appropriate masses for the cluster sample in this work.

The two highest exclusion curves overplotted in Figure 5 represent the mass and redshift above which an individual cluster would be less than 5% likely to be found in a given survey region in 95% of the Λ CDM parameter probability distribution. We plot one exclusion curve for the least likely cluster allowed in a 2500 deg^2 survey and one curve for the least likely cluster allowed in the entire sky. It is clear that, according to the formalism of M11, no cluster in our sample is individually in strong tension with Λ CDM—a conclusion that would still hold if we applied the naive scaling factor of 1/0.78 discussed in Section 4.1 to all the cluster masses.

This result can be compared to the result of Foley et al. (2011), in which the single cluster SPT-CL J2106-5844 is found to be less than 5% likely to exist in the 2500 deg^2 SPT survey region in 32% of the Λ CDM parameter probability distribution. There are some differences in the two analyses, the most important of which is that Foley et al. (2011) use a mass estimate that combines SZ and X-ray data, whereas this work only reports an SZ-derived mass. The central value of the Foley et al. (2011) combined SZ/X-ray mass estimate is 30% higher

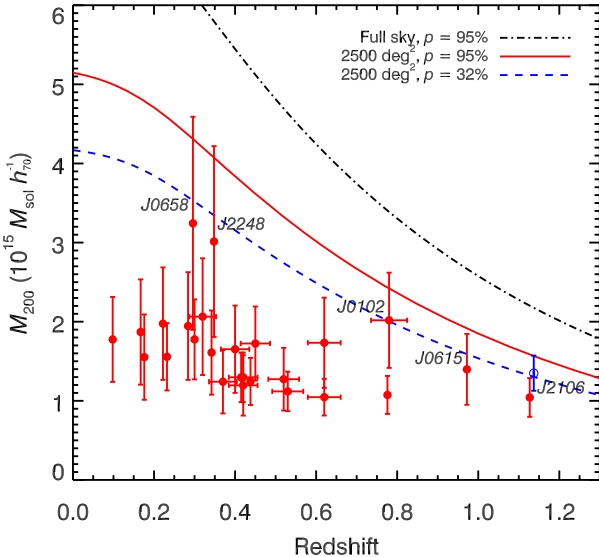


FIG. 5.— An M11-style plot showing the mass $M_{200}(\rho_{\text{mean}})$ and redshift of the clusters presented in this paper. The masses in this plot are slightly ($\sim 5\%$) higher than those presented in Table 6, due to the slightly different treatment of mass bias appropriate to the M11 calculation (see text and M11 for details). Some of the most extreme objects in the catalog are annotated with the R.A. portion of their object name. The red solid line shows the mass above which a cluster at a given redshift is less than 5% likely to be found in the 2500 deg^2 SPT survey region in 95% of the ΛCDM parameter probability distribution. The black dot-dashed line shows the analogous limit for the full sky. The blue open data point (redshift slightly offset for clarity) denotes the mass estimate for SPT-CL J2106-5844 from combined X-ray and SZ measurements in Foley et al. (2011). That work concludes that this cluster is less than 5% likely in 32% of the ΛCDM parameter probability distribution, and we show the corresponding M11 $p = 32\%$ limiting mass vs. redshift as the dashed blue line.

than the central value of the SZ-derived mass reported here. We have included the Foley et al. (2011) combined mass as a point in Figure 5, and we have also plotted the M11 exclusion curve corresponding to $< 5\%$ likelihood of finding a cluster in the SPT survey in 32% of parameter probability. As expected from the result in Foley et al. (2011), the $p = 32\%$ exclusion curve nearly intersects the central SPT-CL J2106-5844 mass value from that work (adjusted appropriately for the M11 plot).

7.2. Extensions to ΛCDM

While no individual cluster lies above either $p = 95\%$ exclusion line in Figure 5, there are several which come reasonably close. One might imagine that the collective “unlikelihood” of these clusters could indicate the need to go beyond the standard ΛCDM cosmological model. The most straightforward extension to ΛCDM that could explain an excess of massive clusters (including ones at high redshift) is the possibility of a non-Gaussian component to the primordial density perturbations. Different models of inflation predict different levels and types of non-Gaussianity (e.g., Bartolo et al. 2004), with the size of the leading-order non-Gaussian term described by the parameter f_{NL} . We have included the mass and redshift distribution of the clusters presented here in a cosmological likelihood calculation with and without f_{NL} as a free parameter. The likelihood calculation was implemented

as in V10, with the effect of f_{NL} on cluster abundance added following the prescription of Dalal et al. (2008). To simplify the selection function and mass scaling part of the calculation, the preview-depth relation (see Table 2) was used for all clusters, and preview-depth values of ξ were estimated for the full-depth clusters by making coadded maps of only one ninth of the observations and running the cluster finder on these maps. As in V10, the scaling relation is not expected to capture the correct behavior at low redshift; as in V10, we exclude this regime by applying a hard cut $z > 0.3$ in this analysis.

The preferred value of f_{NL} in the extended model is consistent with zero ($f_{NL} = 30 \pm 450$ at 68% confidence). We note that this is a significantly weaker constraint than that found by Komatsu et al. (2011) using the CMB bispectrum as measured in the WMAP7 data, but that the two results are consistent with each other and with $f_{NL} = 0$. This is in tension with the recent results of Cayón et al. (2010), Hoyle et al. (2010), and Enqvist et al. (2010), who found significant evidence for non-zero f_{NL} based on other high redshift galaxy clusters using a different statistical technique. In contrast to those works, this analysis uses a likelihood analysis over the full range of mass and redshift space including the SPT selection function, marginalizing over scaling relation uncertainties. This approach naturally incorporates information about both the mass and redshift distribution and the total number of clusters. Our f_{NL} constraints do not change appreciably and are still fully consistent with $f_{NL} = 0$ if we re-run the analysis using a prior on the ξ - M relation that incorporates the scaling between SZ and X-ray masses discussed in Section 4.1.

8. CONCLUSIONS

We have presented a sample of the most massive galaxy clusters in a 2500 deg^2 region of the sky, selected via their SZ signature in SPT observations. These 26 clusters are selected from hundreds of SPT cluster candidates on the basis of their SZ detection significance, which has been shown in previous SPT analyses to correlate tightly with cluster mass (V10, Andersson et al. 2010). As expected from their high SZ significance, each one of these objects shows a strong overdensity of similarly colored galaxies in optical and/or infrared data, and the X-ray luminosity of these systems (as estimated from archival and newly collected data) is consistent with their SZ-derived masses.

We measure (or collect from the literature) photometric—and, in some cases, spectroscopic—redshifts for these 26 clusters. The cluster sample includes several newly discovered high-redshift systems, significantly increasing the total number of known galaxy clusters with masses of $M_{200}(\rho_{\text{mean}}) \gtrsim 10^{15} M_{\odot}$ and redshifts $z \gtrsim 0.5$. In addition to being interesting targets for studies of cluster physics and galaxy formation in the densest environments in the Universe, these massive, high-redshift clusters allow us to test the standard ΛCDM cosmological model with Gaussian initial conditions.

We test whether the most extreme (in mass or redshift) individual clusters pose a challenge to ΛCDM by applying the formalism presented by M11. No single cluster is in significant tension with the ΛCDM model, with the caveat that current SZ mass estimates are uncertain at the 30% level. Improved mass estimates would

strengthen any test of the Λ CDM model. We also examine constraints on primordial non-Gaussianity from the cluster sample. The data show no preference for non-Gaussianity as parametrized by f_{NL} . At 68% confidence, we find $f_{NL} = 20 \pm 450$.

The sample of clusters found with the SPT, the most massive of which are presented in this work, is complementary to the sample expected to be found with the *Planck* satellite. *Planck* will find very massive galaxy clusters over the entire sky—16 times more area than the SPT survey. However, clusters above $z \sim 0.5$ will have a typical angular size of $1'$, meaning that *Planck*'s sensitivity to clusters will fall off at high redshift due to its larger beam ($5'$ FWHM at 150 GHz vs. $1'$ for SPT). The clusters found by *Planck* will thus be distributed towards significantly lower redshift than those found by the SPT.

The SPT observations of the 2500 deg^2 of sky used in this work will be completed to the final survey depth in the Austral winter of 2011. Extrapolating from current survey yields, the complete SPT SZ survey will contain roughly 750 galaxy cluster candidates at a detection significance of $\xi \geq 4.5$ (and over 400 at $\xi \geq 5$), the vast majority of which will correspond to real, massive clusters. This unique, nearly mass-limited cluster sample will offer an unprecedented opportunity to test the Λ CDM cosmological model and the properties of dark energy.

Facilities: Blanco (NEWFIRM), Blanco (MOSAIC), CXO (ACIS), Gemini-S (GMOS), Magellan:Baade (IMACS), Magellan:Clay (LDSS3), Spitzer (IRAC), South Pole Telescope, VLT:Antu (FORS2)

We thank Wayne Hu, Dragan Huterer, Eduardo Rozo, and an anonymous referee for helpful discussions and suggestions, and Ryan Chornock and Wen-fai Fong for assistance during spectroscopic observations.

The South Pole Telescope program is supported by the National Science Foundation through grant ANT-0638937. Partial support is also provided by the NSF Physics Frontier Center grant PHY-0114422 to the Kavli Institute of Cosmological Physics at the University of Chicago, the Kavli Foundation, and the Gordon and

Betty Moore Foundation. This work is based in part on observations obtained with the Spitzer Space Telescope (PID 60099), which is operated by the Jet Propulsion Laboratory, California Institute of Technology under a contract with NASA. Support for this work was provided by NASA through an award issued by JPL/Caltech. Additional data were obtained with the 6.5 m Magellan Telescopes located at the Las Campanas Observatory, Chile. Support for X-ray analysis was provided by NASA through Chandra Award Numbers 12800071 and 12800088 issued by the Chandra X-ray Observatory Center, which is operated by the Smithsonian Astrophysical Observatory for and on behalf of NASA under contract NAS8-03060. Optical imaging data from the Blanco 4 m at Cerro Tololo Interamerican Observatories (programs 2005B-0043, 2009B-0400, 2010A-0441, 2010B-0598) and spectroscopic observations from VLT programs 086.A-0741 and 286.A-5021 and Gemini program GS-2009B-Q-16 were included in this work. We acknowledge the use of the Legacy Archive for Microwave Background Data Analysis (LAMBDA). Support for LAMBDA is provided by the NASA Office of Space Science. Galaxy cluster research at Harvard is supported by NSF grant AST-1009012. Galaxy cluster research at SAO is supported in part by NSF grants AST-1009649 and MRI-0723073. The McGill group acknowledges funding from the National Sciences and Engineering Research Council of Canada, Canada Research Chairs program, and the Canadian Institute for Advanced Research. X-ray research at the CfA is supported through NASA Contract NAS 8-03060. The Munich group acknowledges support from the Excellence Cluster Universe and the DFG research program TR33. R.J.F. is supported by a Clay Fellowship. B.A.B is supported by a KICP Fellowship, support for M.Brodwin was provided by the W. M. Keck Foundation, M.Bautz acknowledges support from contract 2834-MIT-SAO-4018 from the Pennsylvania State University to the Massachusetts Institute of Technology. M.D. acknowledges support from an Alfred P. Sloan Research Fellowship, W.F. and C.J. acknowledge support from the Smithsonian Institution, and B.S. acknowledges support from the Brinson Foundation.

REFERENCES

Abell, G. O., Corwin, Jr., H. G., & Olowin, R. P. 1989, ApJS, 70, 1
 Andersson, K., et al. 2010, submitted to ApJ, arXiv:1006.3068
 Ashby, M. L. N., et al. 2009, ApJ., 701, 428
 Barbosa, D., Bartlett, J., Blanchard, A., & Oukbir, J. 1996, A&A, 314, 13
 Bartolo, N., Komatsu, E., Matarrese, S., & Riotto, A. 2004, Phys. Rep., 402, 103
 Battye, R. A., & Weller, J. 2003, Phys. Rev. D, 68, 083506
 Benson, B. A., et al. 2011, In prep.
 Böhringer, H., et al. 2004a, A&A, 425, 367
 —. 2004b, A&A, 425, 367
 Brodin, M., et al. 2010, ApJ, 721, 90
 Brott, I., & Hauschildt, P. H. 2005, in ESA Special Publication, Vol. 576, The Three-Dimensional Universe with Gaia, ed. C. Turon, K. S. O'Flaherty, & M. A. C. Perryman, 565–+
 Carlstrom, J. E., et al. 2011, PASP, 123, 568
 Carlstrom, J. E., Holder, G. P., & Reese, E. D. 2002, ARA&A, 40, 643
 Cayón, L., Gordon, C., & Silk, J. 2010, ArXiv e-prints, 1006.1950
 Clowe, D., Bradač, M., Gonzalez, A. H., Markevitch, M., Randall, S. W., Jones, C., & Zaritsky, D. 2006, ApJ, 648, L109
 Collister, A. A., & Lahav, O. 2004, PASP, 116, 345
 Covey, K. R., et al. 2007, AJ, 134, 2398
 Dalal, N., Doré, O., Huterer, D., & Shirokov, A. 2008, Phys. Rev. D, 77, 123514
 de Grandi, S., et al. 1999, ApJ, 514, 148
 Duffy, A. R., Schaye, J., Kay, S. T., & Dalla Vecchia, C. 2008, MNRAS, 390, L64
 Eddington, A. S. 1913, MNRAS, 73, 359
 Edge, A. C., et al. 1994, A&A, 289, L34
 Enqvist, K., Hotchkiss, S., & Taanila, O. 2010, ArXiv e-prints, 1012.2732
 Foley, R. J., et al. 2011, ApJ, 731, 86
 Fowler, J. W., et al. 2007, Appl. Opt., 46, 3444
 Haiman, Z., Mohr, J. J., & Holder, G. P. 2001, ApJ, 553, 545
 Hall, N. R., et al. 2010, ApJ, 718, 632
 High, F. W., et al. 2010, ApJ, 723, 1736
 High, F. W., Stubbs, C. W., Rest, A., Stalder, B., & Challis, P. 2009, AJ, 138, 110
 Holder, G., Haiman, Z., & Mohr, J. J. 2001, ApJ, 560, L111
 Holder, G. P., & Carlstrom, J. E. 2001, ApJ, 558, 515, astro-ph/0105229
 Hoyle, B., Jimenez, R., & Verde, L. 2010, ArXiv e-prints, 1009.3884
 Komatsu, E., et al. 2011, ApJS, 192, 18

Larson, D., et al. 2011, *ApJS*, 192, 16

Lee, S., Gildemeister, J. M., Holmes, W., Lee, A. T., & Richards, P. L. 1998, *Appl. Opt.*, 37, 3391

Lima, M., & Hu, W. 2007, *Phys. Rev. D*, 76, 123013

Mantz, A., Allen, S. W., Ebeling, H., Rapetti, D., & Drlica-Wagner, A. 2010, *MNRAS*, 406, 1773

Marriage, T. A., et al. 2011, *ApJ*, 731, 100

Matarrese, S., Verde, L., & Jimenez, R. 2000, *ApJ*, 541, 10

Melin, J.-B., Bartlett, J. G., & Delabrouille, J. 2006, *A&A*, 459, 341

Menanteau, F., et al. 2010, *ApJ*, 723, 1523

Mohr, J. J., et al. 2008, in Society of Photo-Optical Instrumentation Engineers (SPIE) Conference Series, Vol. 7016, Society of Photo-Optical Instrumentation Engineers (SPIE) Conference Series

Molnar, S. M., Haiman, Z., Birkinshaw, M., & Mushotzky, R. F. 2004, *ApJ*, 601, 22

Mortenson, M. J., Hu, W., & Huterer, D. 2011, *Phys. Rev. D*, 83, 023015

Motl, P. M., Hallman, E. J., Burns, J. O., & Norman, M. L. 2005, *ApJ*, 623, L63

Nagai, D., Kravtsov, A. V., & Vikhlinin, A. 2007, *ApJ*, 668, 1

Ngeow, C., et al. 2006, in Society of Photo-Optical Instrumentation Engineers (SPIE) Conference Series, Vol. 6270, Society of Photo-Optical Instrumentation Engineers (SPIE) Conference Series

Percival, W. J., et al. 2010, *MNRAS*, 401, 2148

Pratt, G. W., Croston, J. H., Arnaud, M., & Böhringer, H. 2009, *A&A*, 498, 361

Riess, A. G., et al. 2009, *ApJ*, 699, 539

Rozo, E., et al. 2010, *ApJ*, 708, 645

Schlegel, D. J., Finkbeiner, D. P., & Davis, M. 1998, *ApJ*, 500, 525

Sehgal, N., Bode, P., Das, S., Hernandez-Monteagudo, C., Huffenberger, K., Lin, Y., Ostriker, J. P., & Trac, H. 2010a, *ApJ*, 709, 920

Sehgal, N., et al. 2010b, ArXiv e-prints, 1010.1025

Shaw, L. D., Holder, G. P., & Bode, P. 2008, *ApJ*, 686, 206

Shaw, L. D., Zahn, O., Holder, G. P., & Doré, O. 2009, *ApJ*, 702, 368

Shirokoff, E., et al. 2011, *ApJ*, in press, arXiv:1012.4788

Stanek, R., Rasia, E., Evrard, A. E., Pearce, F., & Gazzola, L. 2009, ArXiv e-prints, 0910.1599

Staniszewski, Z., et al. 2009, *ApJ*, 701, 32

Struble, M. F., & Rood, H. J. 1999, *ApJS*, 125, 35

Sunyaev, R. A., & Zel'dovich, Y. B. 1972, *Comments on Astrophysics and Space Physics*, 4, 173

Tinker, J., Kravtsov, A. V., Klypin, A., Abazajian, K., Warren, M., Yepes, G., Gottlöber, S., & Holz, D. E. 2008, *ApJ*, 688, 709

Tucker, W., et al. 1998, *ApJ*, 496, L5

Vanderlinde, K., et al. 2010, *ApJ*, 722, 1180

Vikhlinin, A., et al. 2009a, *ApJ*, 692, 1033

—. 2009b, *ApJ*, 692, 1060

Vikhlinin, A., McNamara, B., Forman, W., Jones, C., Quintana, H., & Hornstrup, A. 1998, *ApJ*, 502, 558

Voges, W., et al. 1999, *A&A*, 349, 389

Wang, L., & Steinhardt, P. J. 1998, *ApJ*, 508, 483

Wang, S., Khouri, J., Haiman, Z., & May, M. 2004, *Phys. Rev. D*, 70, 123008

TABLE 6
CLUSTERS

| Object Name | R.A. | decl. | ξ | Depth | z | $M_{200} \pm \text{stat} \pm \text{syst}$ [$10^{14} M_{\odot} h_{70}^{-1}$] | $M_{500} \pm \text{stat} \pm \text{syst}$ [$10^{14} M_{\odot} h_{70}^{-1}$] | F_{X} [$10^{-3} \text{ ergs cm}^{-2} \text{ s}^{-1}$] | L_{X} [$10^{44} \text{ ergs s}^{-1}$] |
|---------------------------------|---------|---------|-------|---------|-----------|--|--|---|---|
| SPT-CL J0040-4407 | 10.202 | -44.131 | 10.1 | shallow | 0.40 (p) | 15.9 \pm 2.3 \pm 4.1 | 7.8 \pm 2.0 \pm 2.0 | 7.2 \pm 2.6 | 3.5 \pm 1.2 |
| SPT-CL J0102-4915 ¹ | 15.728 | -49.257 | 39.5 | full | 0.78 (p) | 18.9 \pm 2.9 \pm 3.5 | 9.9 \pm 2.5 \pm 1.8 | 6.1 \pm 2.1 | 11.3 \pm 3.9 |
| SPT-CL J0232-4421 ² | 38.070 | -44.351 | 11.4 | shallow | 0.284 (s) | 18.8 \pm 2.6 \pm 5.3 | 8.9 \pm 2.2 \pm 2.4 | 30.3 \pm 3.3 | 6.4 \pm 0.7 |
| SPT-CL J0234-5831 | 38.670 | -58.520 | 14.7 | full | 0.415 (s) | 12.4 \pm 2.0 \pm 1.7 | 6.2 \pm 1.7 \pm 0.8 | 11.6 \pm 2.9 | 5.6 \pm 1.4 |
| SPT-CL J0243-4833 | 40.910 | -48.557 | 13.8 | full | 0.53 (p) | 10.7 \pm 1.8 \pm 1.4 | 5.5 \pm 1.5 \pm 0.7 | 9.1 \pm 1.8 | 7.4 \pm 1.5 |
| SPT-CL J0245-5302 ³ | 41.378 | -53.036 | 19.3 | full | 0.300 (s) | 17.0 \pm 2.7 \pm 3.2 | 8.1 \pm 2.1 \pm 1.5 | 16.2 \pm 2.1 | 7.2 \pm 0.9 |
| SPT-CL J0254-5856 | 43.563 | -58.949 | 14.3 | full | 0.438 (s) | 11.9 \pm 1.9 \pm 1.7 | 6.0 \pm 1.6 \pm 0.8 | 13.5 \pm 2.8 | 7.2 \pm 1.5 |
| SPT-CL J0304-4401 | 46.064 | -44.030 | 8.0 | shallow | 0.52 (p) | 12.1 \pm 2.0 \pm 2.6 | 6.2 \pm 1.7 \pm 1.3 | 8.9 \pm 1.8 | 7.0 \pm 1.4 |
| SPT-CL J0411-4819 | 62.811 | -48.321 | 14.8 | full | 0.42 (p) | 12.4 \pm 2.0 \pm 1.7 | 6.2 \pm 1.7 \pm 0.8 | 11.9 \pm 3.4 | 6.0 \pm 1.8 |
| SPT-CL J0417-4748 | 64.340 | -47.812 | 13.9 | full | 0.62 (p) | 10.0 \pm 1.6 \pm 1.2 | 5.2 \pm 1.4 \pm 0.6 | 4.8 \pm 0.8 | 5.5 \pm 0.9 |
| SPT-CL J0438-5411 ⁴ | 69.569 | -54.321 | 22.3 | full | 0.45 (p) | 16.5 \pm 2.6 \pm 2.8 | 8.2 \pm 2.1 \pm 1.4 | 18.8 \pm 3.0 | 10.7 \pm 1.7 |
| SPT-CL J0549-6204 | 87.326 | -62.083 | 12.6 | shallow | 0.32 (p) | 19.9 \pm 2.7 \pm 6.1 | 9.5 \pm 2.3 \pm 2.8 | 25.2 \pm 1.4 | 6.9 \pm 0.4 |
| SPT-CL J0555-6405 | 88.851 | -64.099 | 7.1 | shallow | 0.42 (p) | 11.3 \pm 2.1 \pm 2.8 | 5.6 \pm 1.6 \pm 1.4 | 9.5 \pm 0.6 | 4.7 \pm 0.3 |
| SPT-CL J0615-5746 | 93.957 | -57.778 | 11.1 | shallow | 0.972 (s) | 13.2 \pm 1.9 \pm 3.5 | 7.1 \pm 1.8 \pm 1.8 | 4.3 \pm 0.7 | 12.6 \pm 2.1 |
| SPT-CL J0628-4143 ⁵ | 97.201 | -41.720 | 8.1 | shallow | 0.176 (s) | 14.9 \pm 2.5 \pm 4.0 | 6.9 \pm 1.9 \pm 1.8 | 30.0 \pm 2.7 | 2.3 \pm 0.2 |
| SPT-CL J0638-5358 ⁶ | 99.693 | -53.974 | 11.1 | shallow | 0.222 (s) | 19.1 \pm 2.7 \pm 5.6 | 8.9 \pm 2.2 \pm 2.5 | 44.0 \pm 3.1 | 5.5 \pm 0.4 |
| SPT-CL J0645-5413 ⁷ | 101.360 | -54.224 | 10.0 | shallow | 0.167 (s) | 18.1 \pm 2.7 \pm 5.4 | 8.3 \pm 2.1 \pm 2.4 | 53.7 \pm 4.1 | 3.7 \pm 0.3 |
| SPT-CL J0658-5556 ⁸ | 104.625 | -55.949 | 22.0 | shallow | 0.296 (s) | 31.2 \pm 3.9 \pm 10.8 | 14.6 \pm 3.4 \pm 4.9 | 44.0 \pm 3.5 | 10.1 \pm 0.8 |
| SPT-CL J2023-5535 ⁹ | 305.833 | -55.590 | 14.8 | full | 0.232 (s) | 14.9 \pm 2.4 \pm 2.7 | 7.0 \pm 1.9 \pm 1.2 | 19.2 \pm 3.5 | 2.6 \pm 0.5 |
| SPT-CL J2031-4037 ¹⁰ | 307.960 | -40.619 | 9.4 | shallow | 0.342 (s) | 15.5 \pm 2.3 \pm 4.3 | 7.5 \pm 1.9 \pm 2.0 | 20.6 \pm 4.8 | 6.5 \pm 1.5 |
| SPT-CL J2106-5844 | 316.515 | -58.744 | 22.1 | full | 1.132 (s) | 9.8 \pm 1.5 \pm 1.4 | 5.4 \pm 1.4 \pm 0.7 | 2.0 \pm 0.2 | 13.9 \pm 1.0 |
| SPT-CL J2201-5956 ¹¹ | 330.462 | -59.944 | 14.5 | full | 0.098 (s) | 17.0 \pm 2.8 \pm 3.7 | 7.6 \pm 2.0 \pm 1.6 | 125.2 \pm 8.1 | 2.8 \pm 0.2 |
| SPT-CL J2248-4431 ¹² | 342.181 | -44.527 | 20.7 | shallow | 0.348 (s) | 29.0 \pm 3.7 \pm 9.6 | 13.8 \pm 3.2 \pm 4.4 | 54.1 \pm 6.1 | 17.7 \pm 2.0 |
| SPT-CL J2325-4111 ¹³ | 351.294 | -41.194 | 7.2 | shallow | 0.37 (p) | 11.8 \pm 2.1 \pm 3.0 | 5.8 \pm 1.7 \pm 1.4 | 15.0 \pm 4.1 | 5.6 \pm 1.5 |
| SPT-CL J2337-5942 | 354.347 | -59.703 | 16.8 | full | 0.775 (s) | 10.2 \pm 1.6 \pm 1.2 | 5.4 \pm 1.4 \pm 0.6 | 3.1 \pm 0.2 | 8.9 \pm 0.5 |
| SPT-CL J2344-4243 | 356.176 | -42.719 | 12.1 | shallow | 0.62 (p) | 16.6 \pm 2.3 \pm 4.4 | 8.5 \pm 2.1 \pm 2.2 | 18.3 \pm 5.5 | 21.1 \pm 6.3 |

NOTE. — ξ is the maximum signal-to-noise obtained over the set of filter scales. z is the redshift where (s) refers to a spectral redshift and (p) refers to a photometric redshift. Table 3 shows a detailed breakdown of the redshift observation. The masses $M_{500}(\rho_{crit})$ (where the overdensity is with respect to the critical density rather than the mean density) were calculated by converting from $M_{200}(\rho_{mean})$ assuming an NFW density profile and the mass-concentration relation of Duffy et al. (2008). The X-ray Flux and Luminosity are reported for the 0.5-2.0 keV band in the cluster frame.

¹ ACT-CL J0102-4915

² RXC J0232-24420

³ ABELL S0295, ACT-CL J0245-5302

⁴ ACT-CL J0438-5419

⁵ ABELL 3396, RXC J0628-84143

⁶ ABELL S0592, RXC J0638-7-3358, ACT-CL J0638-5358

⁷ ABELL 3404, RXC J0645.4-5413, ACT-CL J0645-5413

⁸ Bullet, RXC J0658.5-5556, ACT-CL J0658-5557

⁹ RXC J2023-4-5335

¹⁰ RXC J2031-8-4037

¹¹ ABELL 3827, RXC J2201-9-5956

¹² ABELL S1063, RXC J2248.7-4431

¹³ ABELL S1121

APPENDIX
SZ AND OPTICAL/INFRARED IMAGES

Figures 6–31 show SZ detection significance maps (*left panels*) and optical and infrared images (*right panels*) of the clusters. In all images, north is up, east is left. The SZ-only insets subtend 12 arcminutes on a side. The mapping between color and SZ significance ξ is different in all SZ thumbnails, spanning the full range of SZ pixel values in the region of sky shown. The peak value in each thumbnail is equal to the quoted SZ detection significance in Table 6. Contours denote significance values of $(-8, -4, -2, 0, 2, 4, 8, 16, 32)$ in all thumbnails. Contours are dashed where ξ is negative, and solid where ξ is positive. The negative lobes around some of the most significantly detected clusters in the SZ images are due to the filtering of the time-ordered data and the maps

The optical/infrared images have the same contours as their corresponding SZ thumbnail overlaid. False-color composites are presented for clusters where multiband imaging is available, either from our own observations or from public archives. Otherwise, black-and-white images are shown.

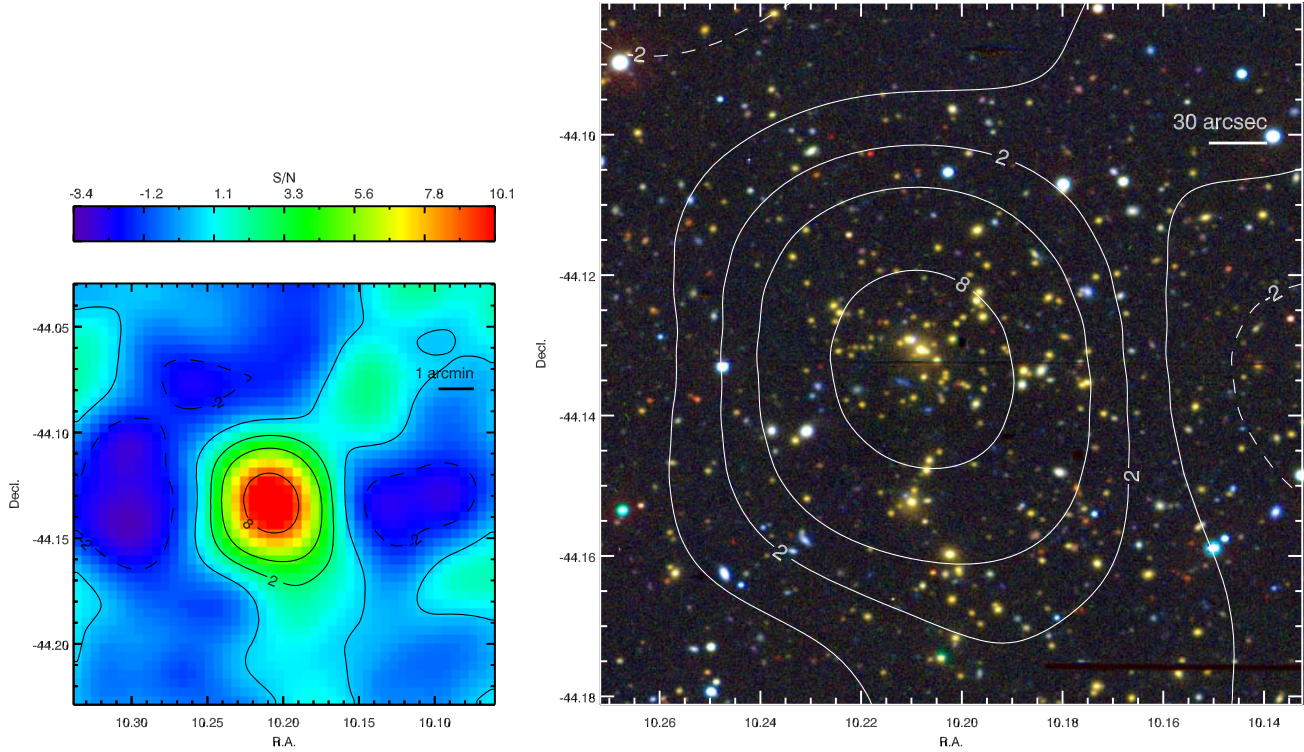


FIG. 6.— SPT-CL J0040-4407 at $z_{rs} = 0.40$. Blanco/MOSAIC-II *irg* images are shown in the optical/infrared panel.

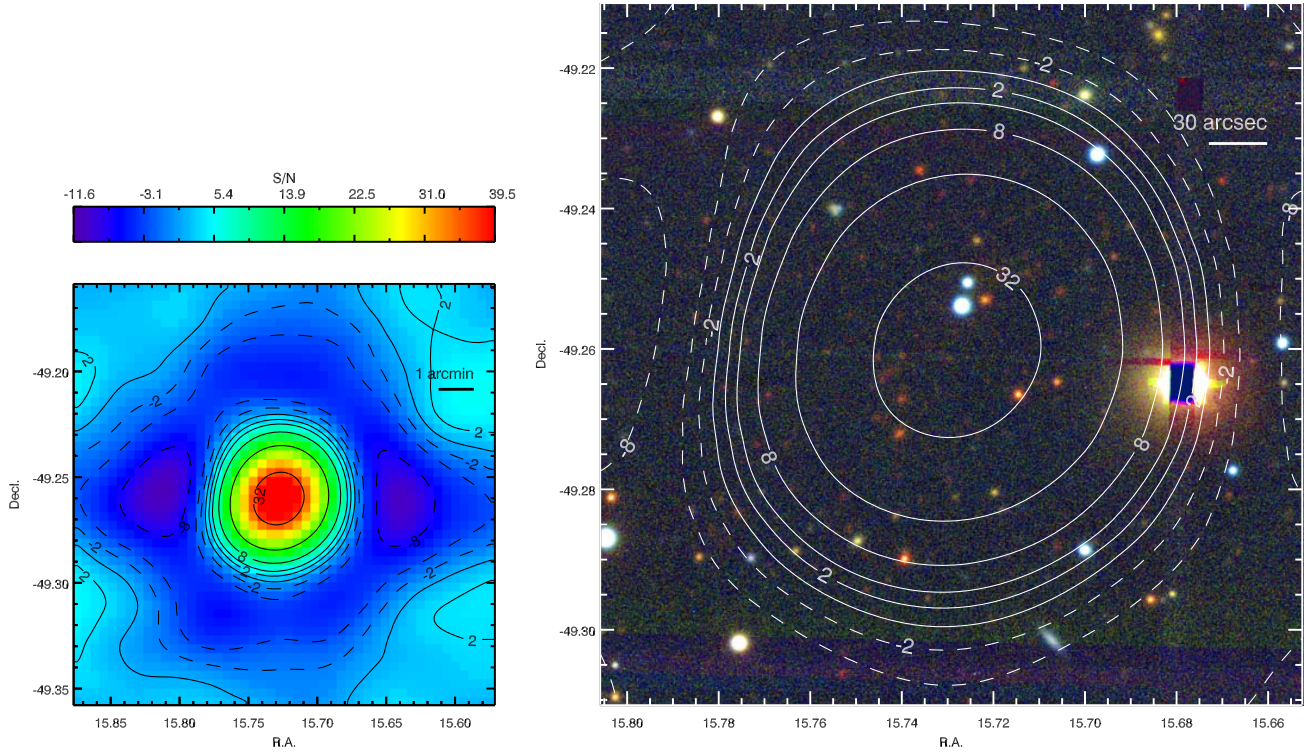


FIG. 7.— SPT-CL J0102-4915, also known as ACT-CL J0102-4915, at $z_{rs} = 0.78$. Blanco/MOSAIC-II *irg* images are shown in the optical/infrared panel.

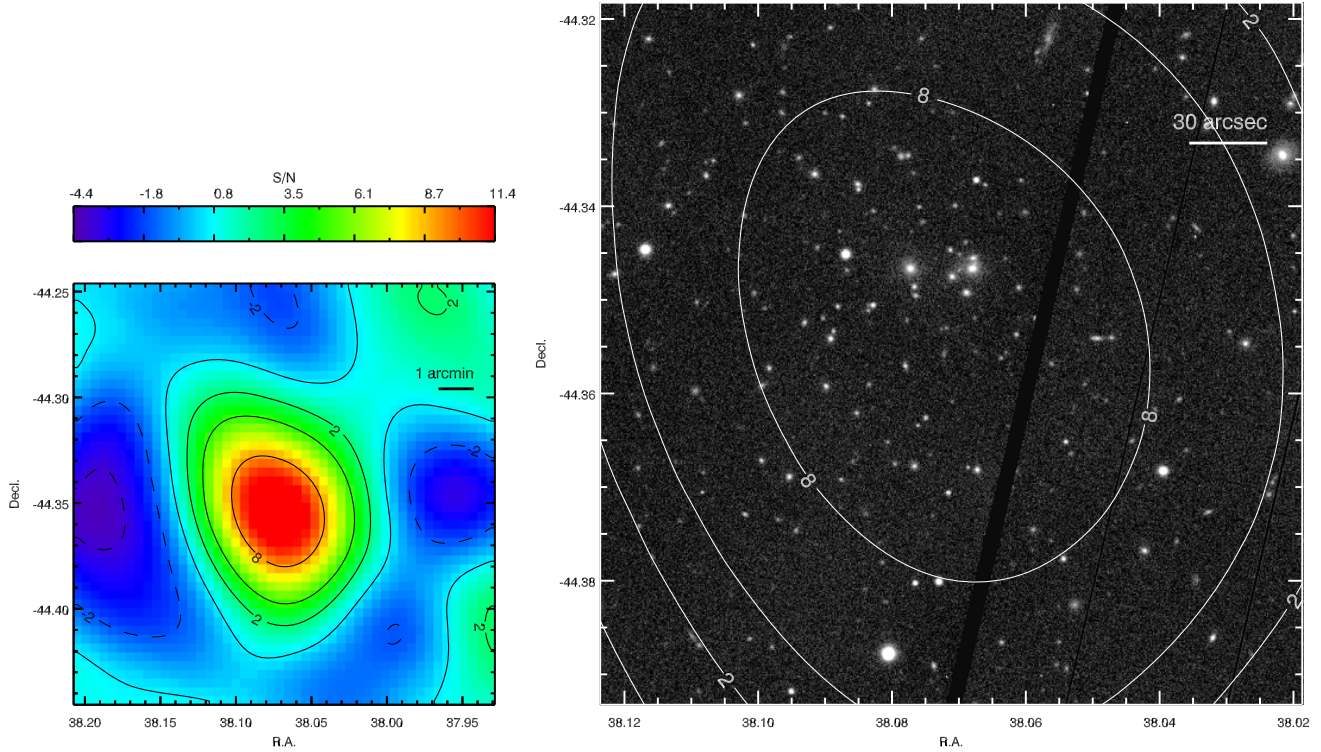


FIG. 8.— SPT-CL J0232-4421, also known as RXC J0232.2-4420, at $z_{\text{spec}} = 0.284$. A VLT/FORS2 R image is shown in the optical/infrared panel

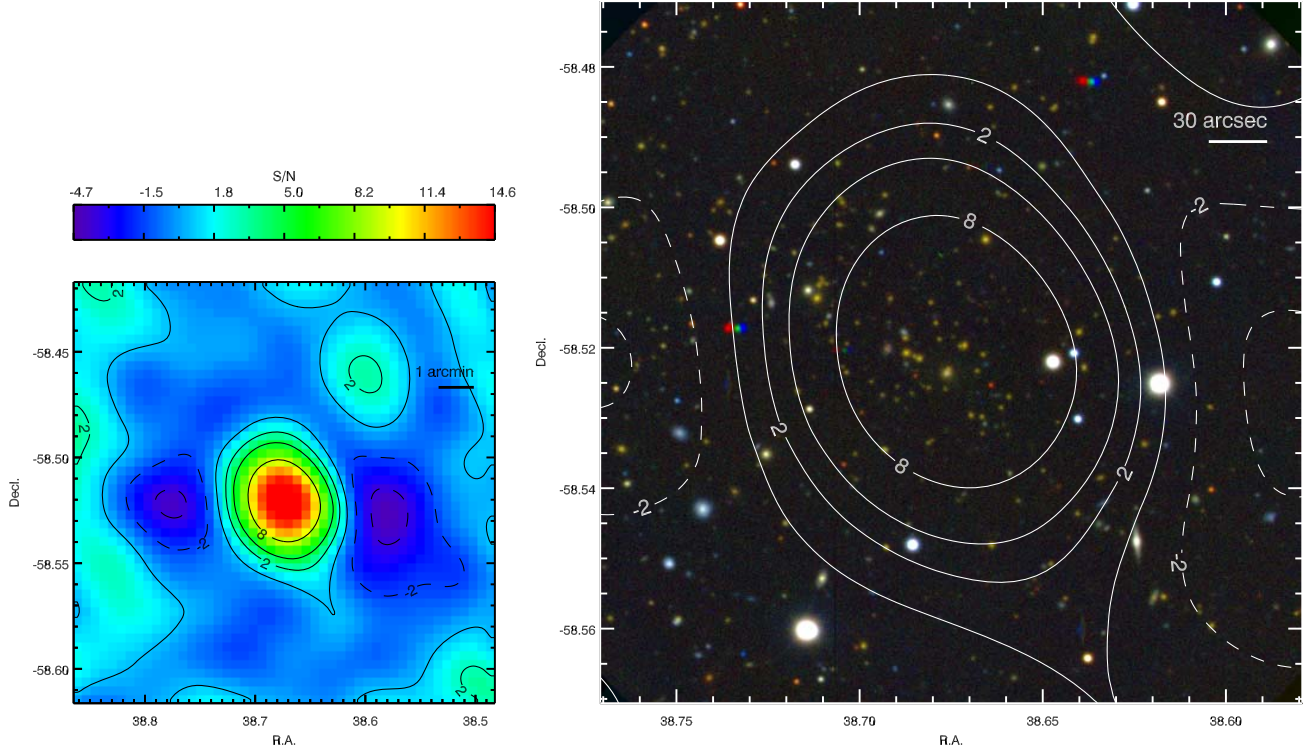


FIG. 9.— SPT-CL J0234-5831 at $z_{\text{spec}} = 0.415$. Magellan/LDSS3 zrg images are shown in the optical/infrared panel.

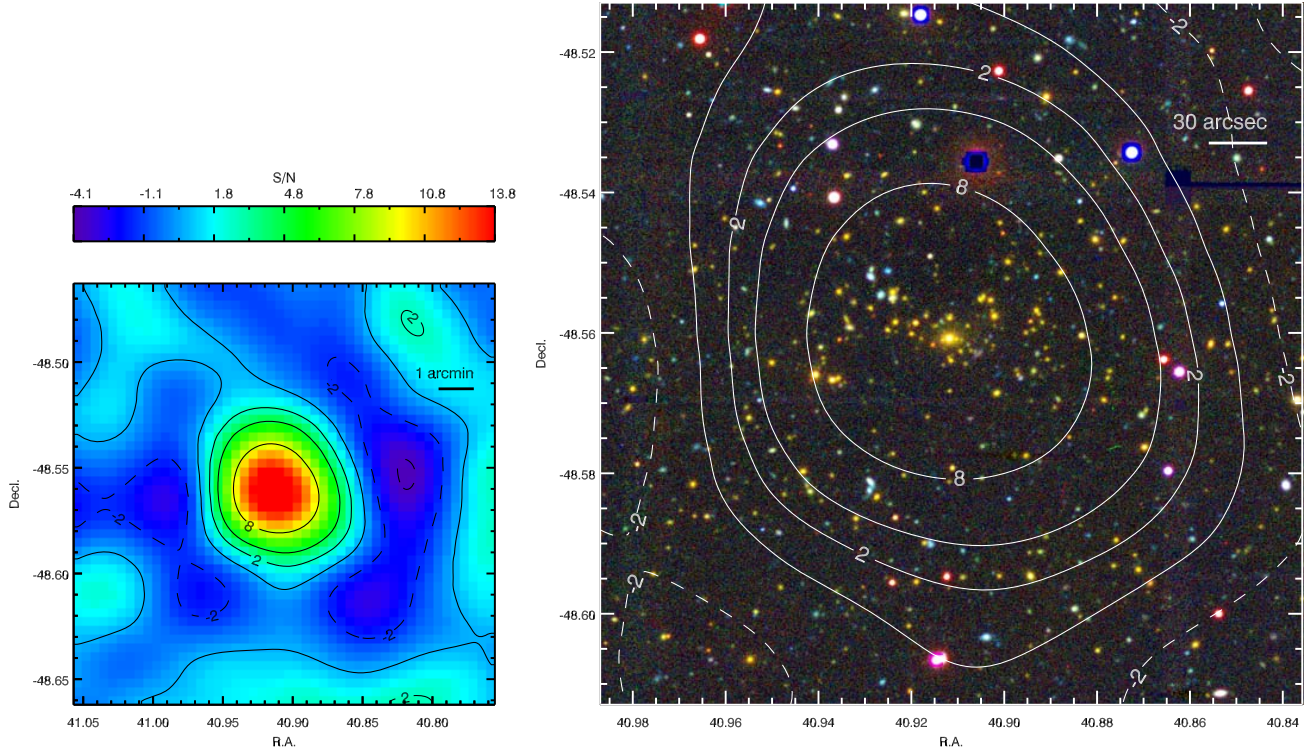


FIG. 10.— SPT-CL J0243-4833 at $z_{rs} = 0.44$. Blanco/MOSAIC-II *irg* images are shown in the optical/infrared panel.

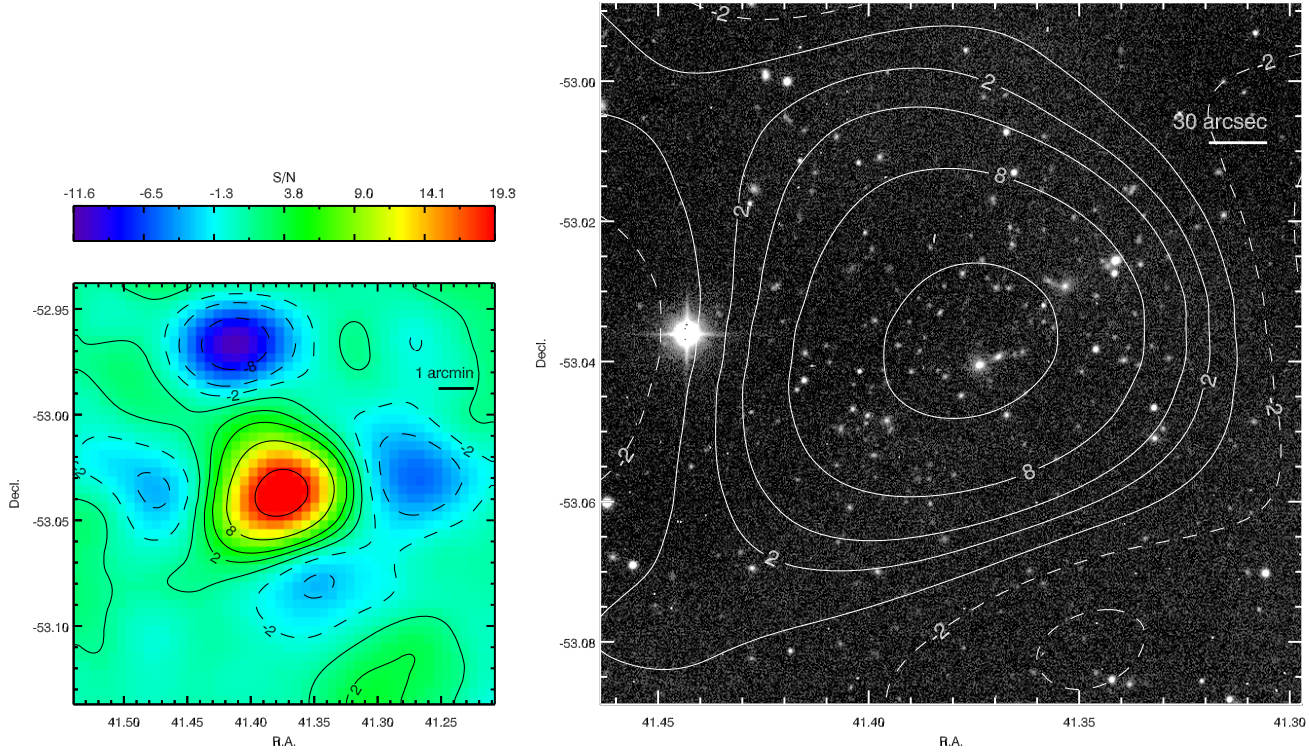


FIG. 11.— SPT-CL J0245-5302, also known as Abell S0295 and ACT-CL J0245-5302, at $z_{spec} = 0.300$. A Swope *R* image is shown in the optical/infrared panel. The stronger of the two point sources discussed in §3.2 is visible as an 11σ negative peak approximately five arcminutes north of the cluster.

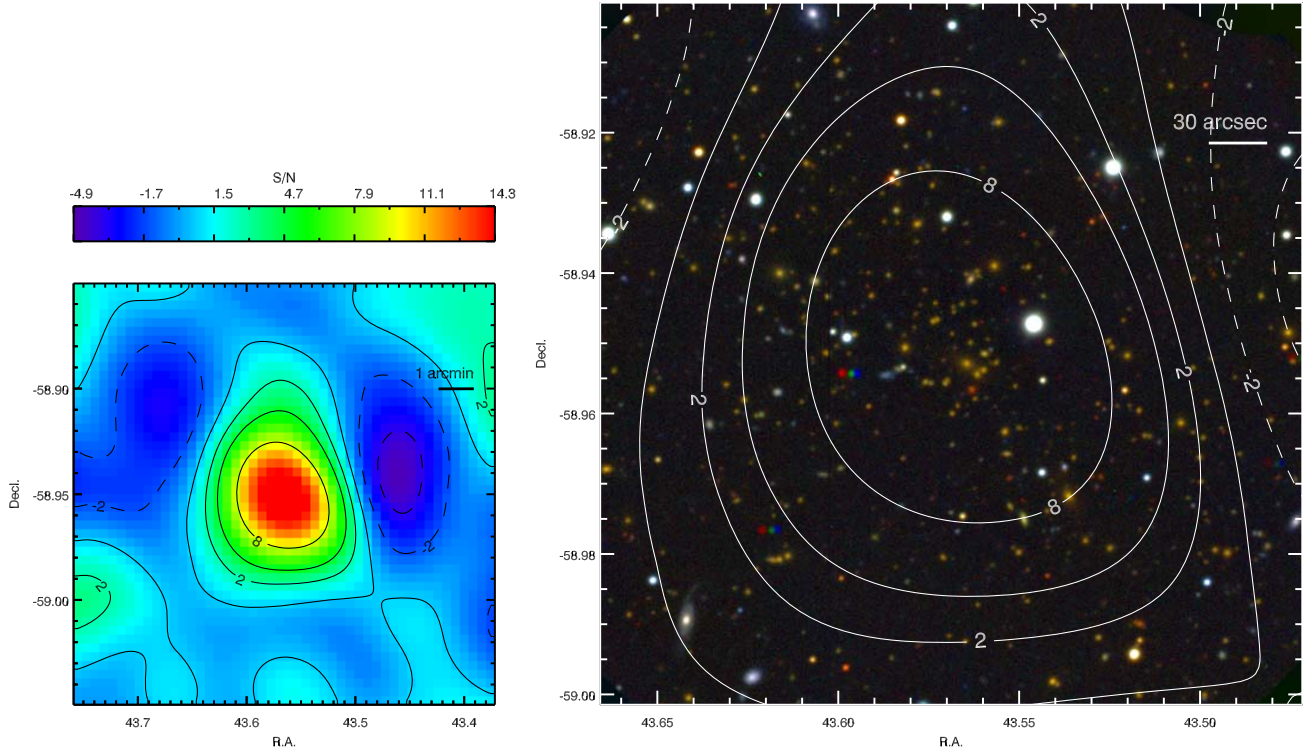


FIG. 12.— SPT-CL J0254-5856 at $z_{\text{spec}} = 0.438$. Magellan/LDSS3 zrg images are shown in the optical/infrared panel.

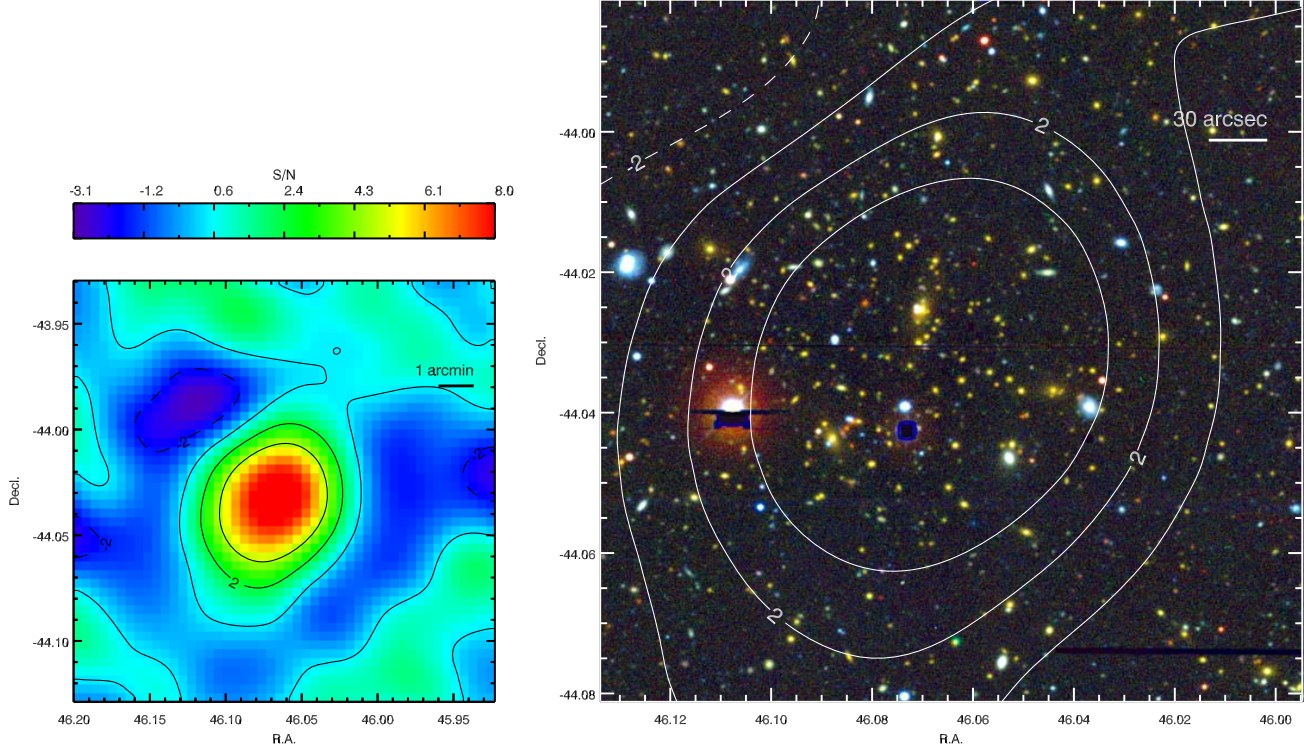


FIG. 13.— SPT-CL J0304-4401 at $z_{\text{rs}} = 0.52$. Blanco/MOSAIC-II irg images are shown in the optical/infrared panel.

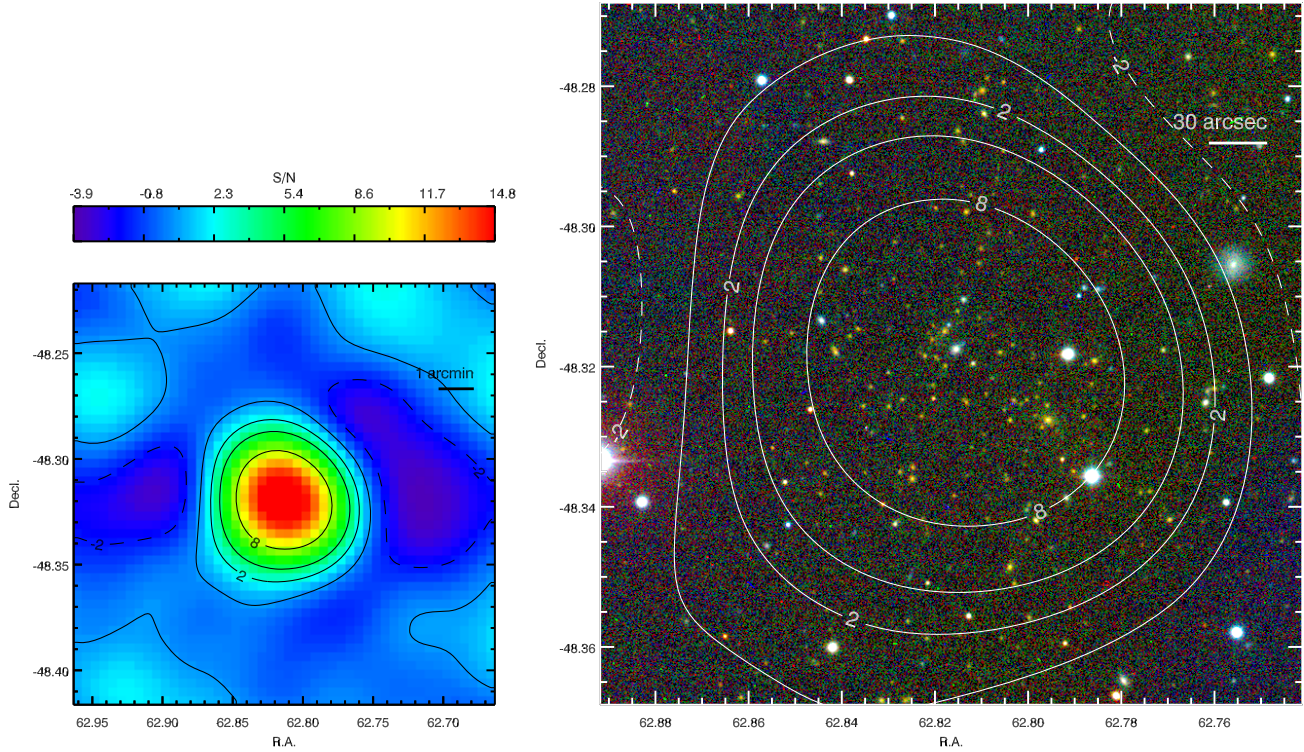


FIG. 14.— SPT-CL J0411-4819 at $z_{rs} = 0.42$. Swope *IRV* images are shown in the optical/infrared panel.

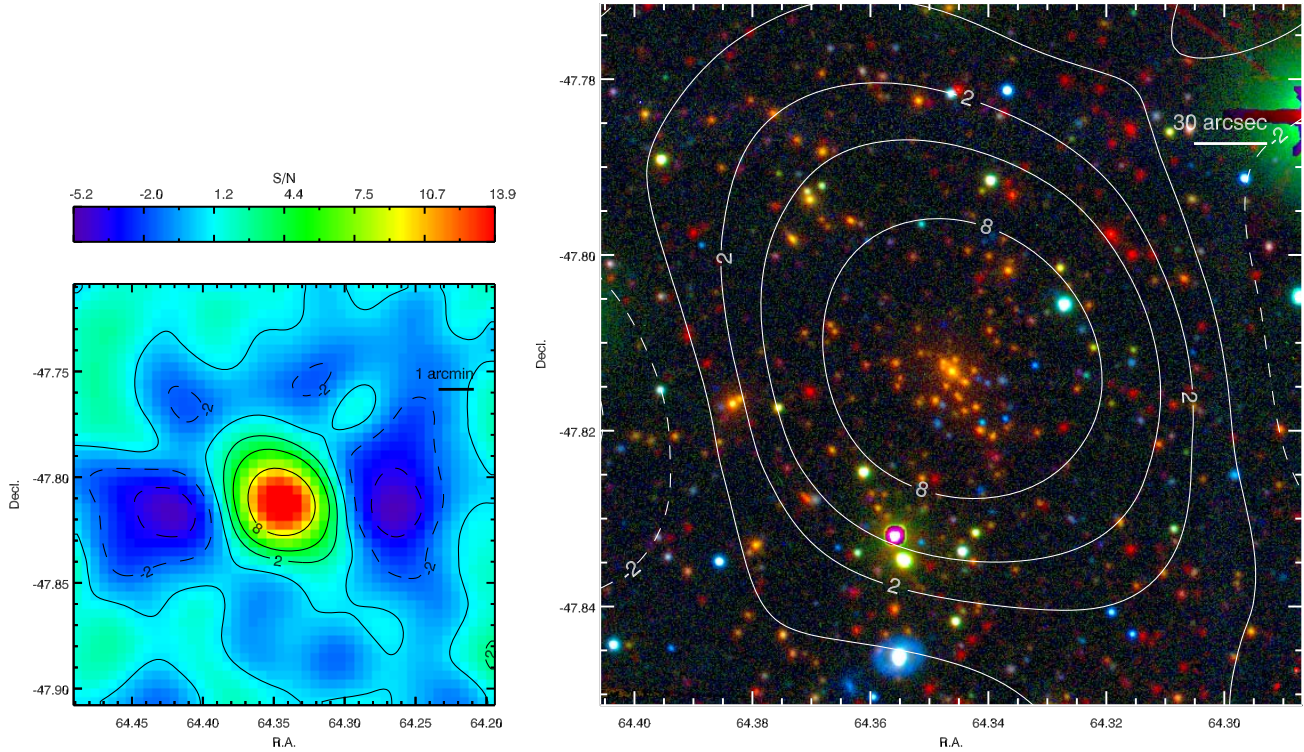


FIG. 15.— SPT-CL J0417-4748 at $z_{rs} = 0.62$. Spitzer/IRAC [3.6] and Blanco/MOSAIC-II *ig* images are shown in the optical/infrared panel.

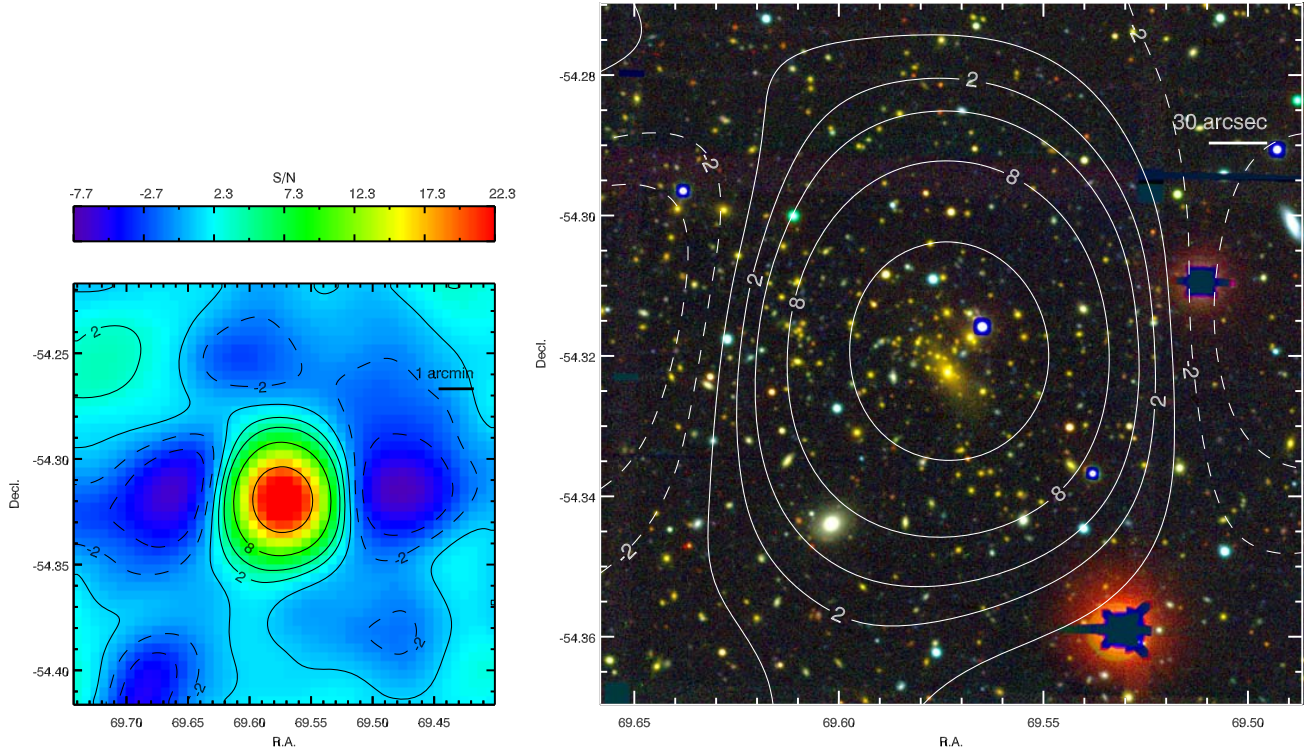


FIG. 16.— SPT-CL J0438-5419, also known as ACT-CL J0438-5419, at $z_{\text{rs}} = 0.45$. Blanco/MOSAIC-II *irg* images are shown in the optical/infrared panel.

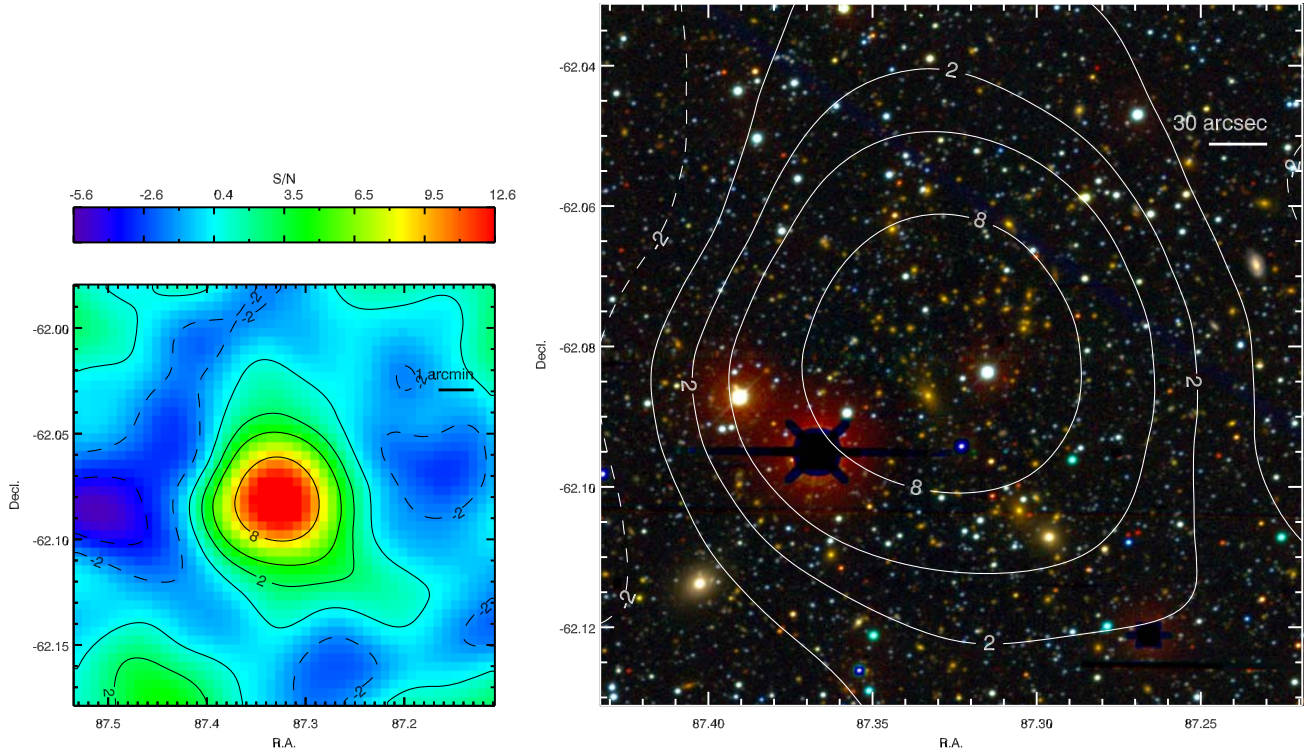


FIG. 17.— SPT-CL J0549-6204 at $z_{\text{rs}} = 0.32$. Blanco/MOSAIC-II *irg* images are shown in the optical/infrared panel.

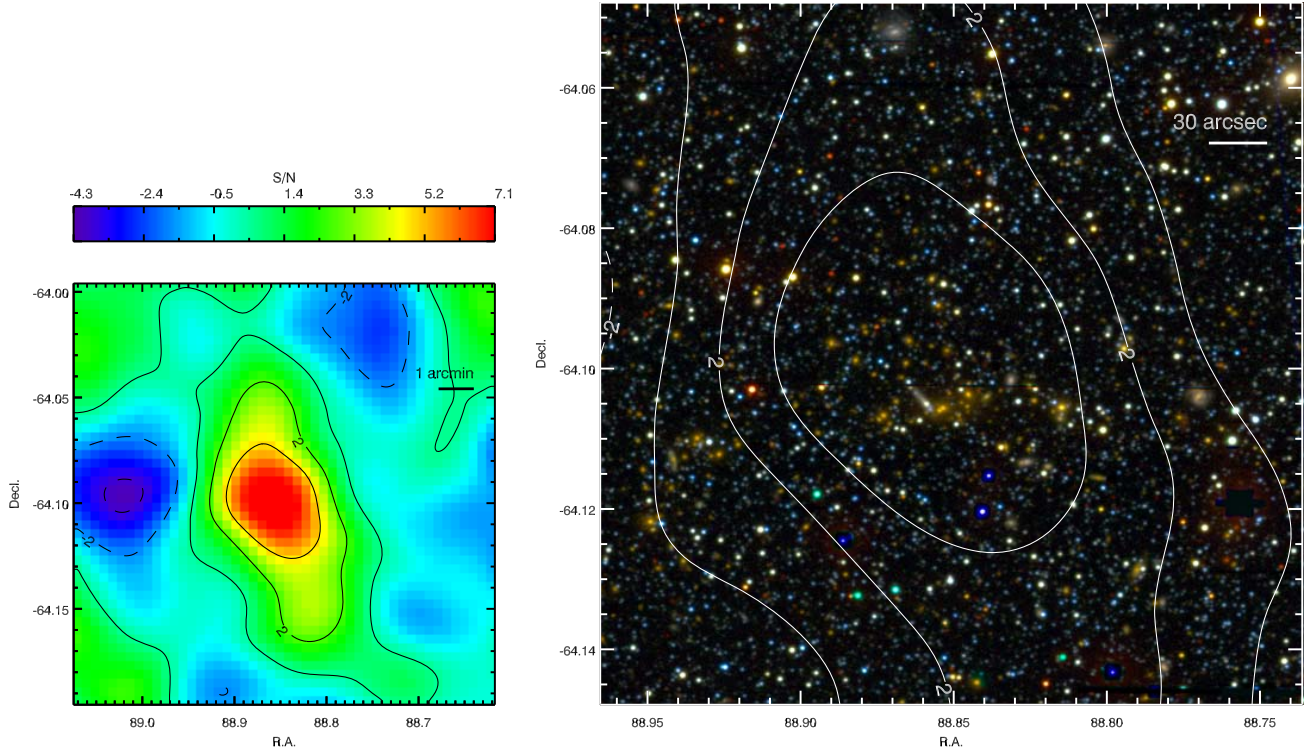


FIG. 18.— SPT-CL J0555-6405 at $z_{rs} = 0.42$. Blanco/MOSAIC-II *irg* images are shown in the optical/infrared panel.

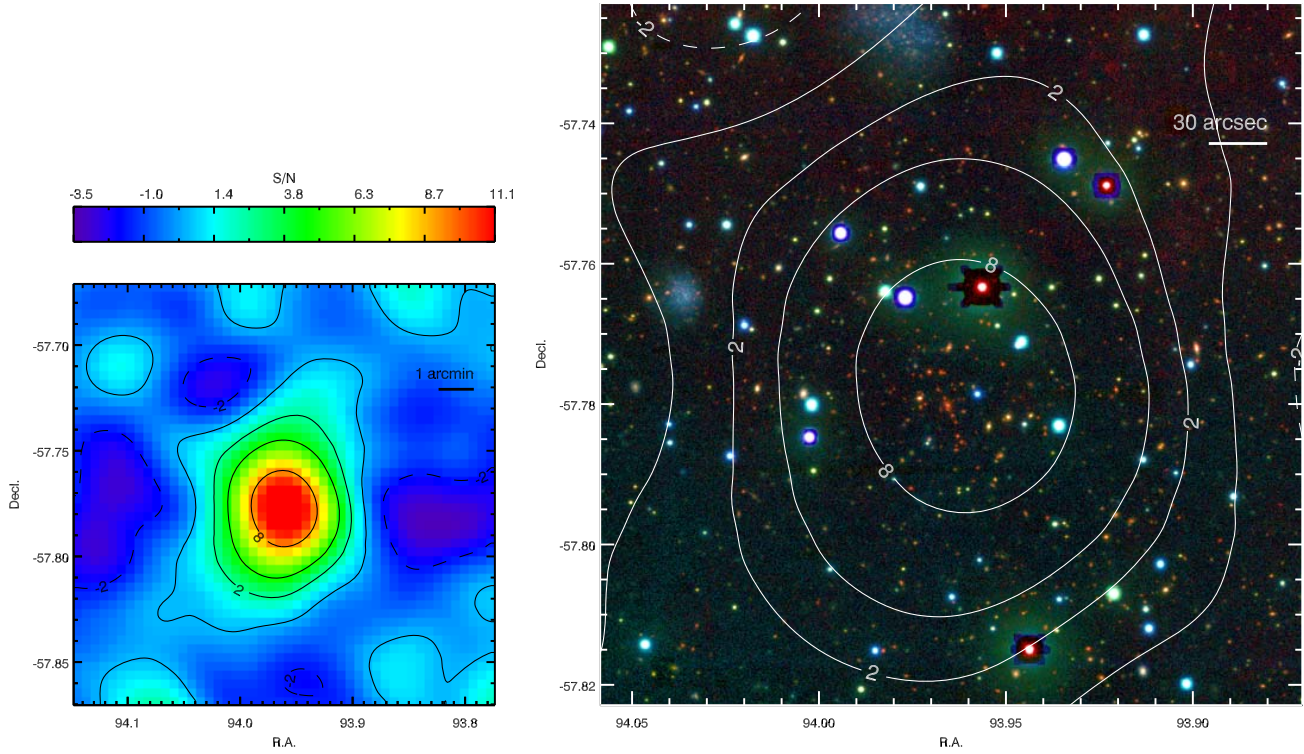


FIG. 19.— SPT-CL J0615-5746 at $z_{spec} = 0.972$. Blanco/NEWFIRM K_s and Blanco/MOSAIC-II rg images are shown in the optical/infrared panel.

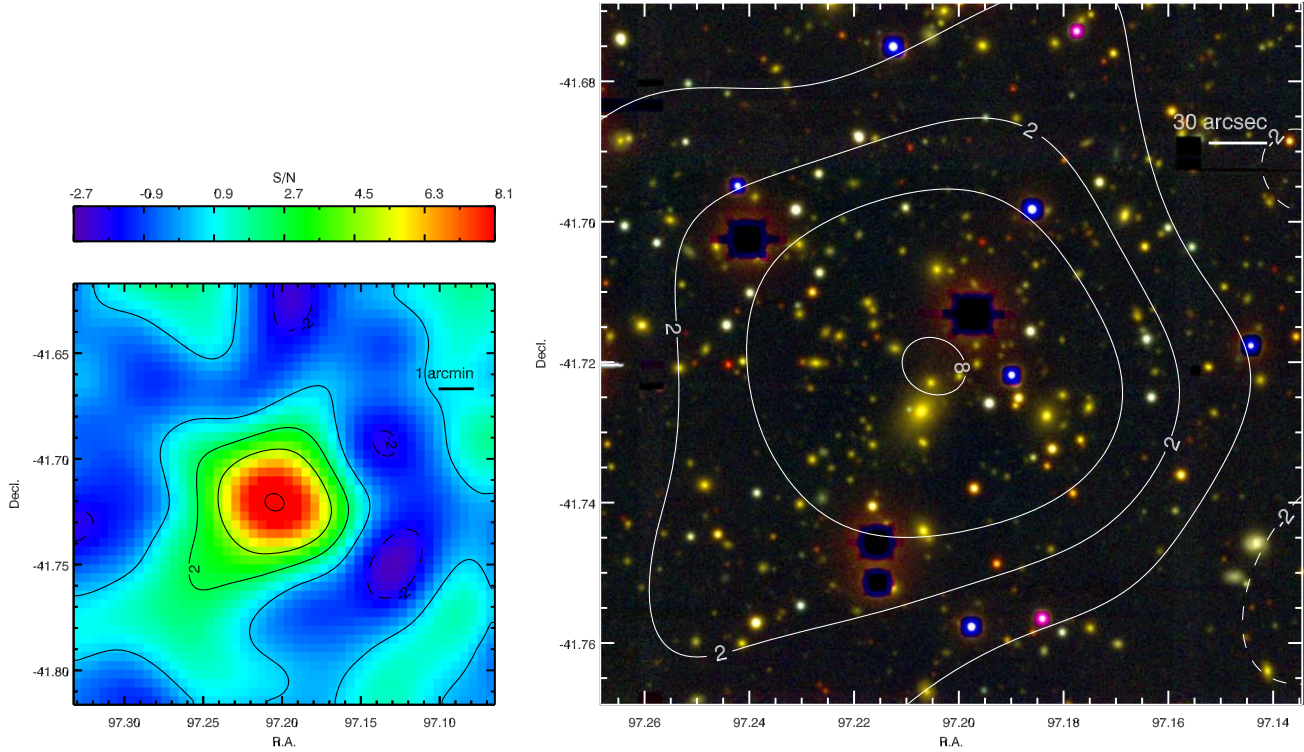


FIG. 20.— SPT-CL J0628-4143, also known as Abell 3396 and RXCJ0628.8-4143, at $z_{\text{spec}} = 0.176$. Blanco/MOSAIC-II *irg* images are shown in the optical/infrared panel.

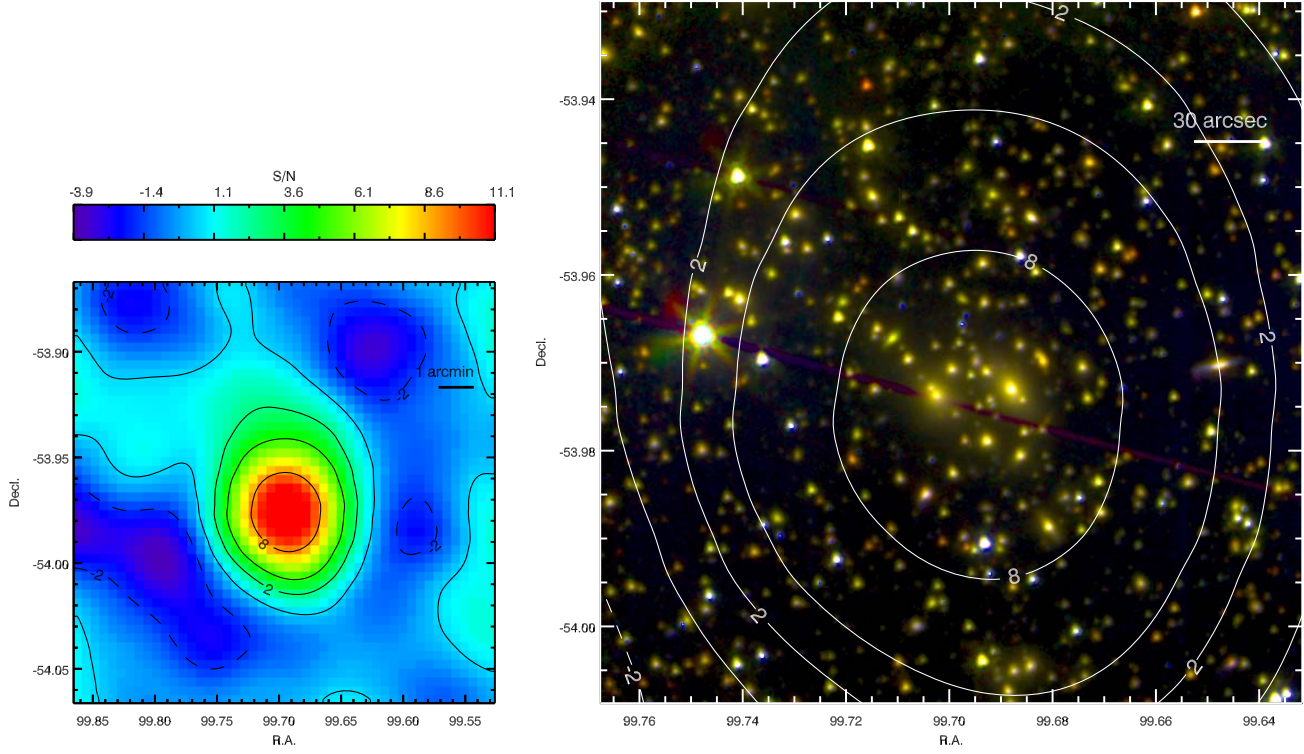


FIG. 21.— SPT-CL J0638-5358, also known as ABELL S0592, RXCJ0638.7-5358, and ACT-CL J0638-5358, at $z_{\text{spec}} = 0.222$. Spitzer/IRAC [4.5][3.6] and Gemini/GMOS *r* images are shown in the optical/infrared panel.

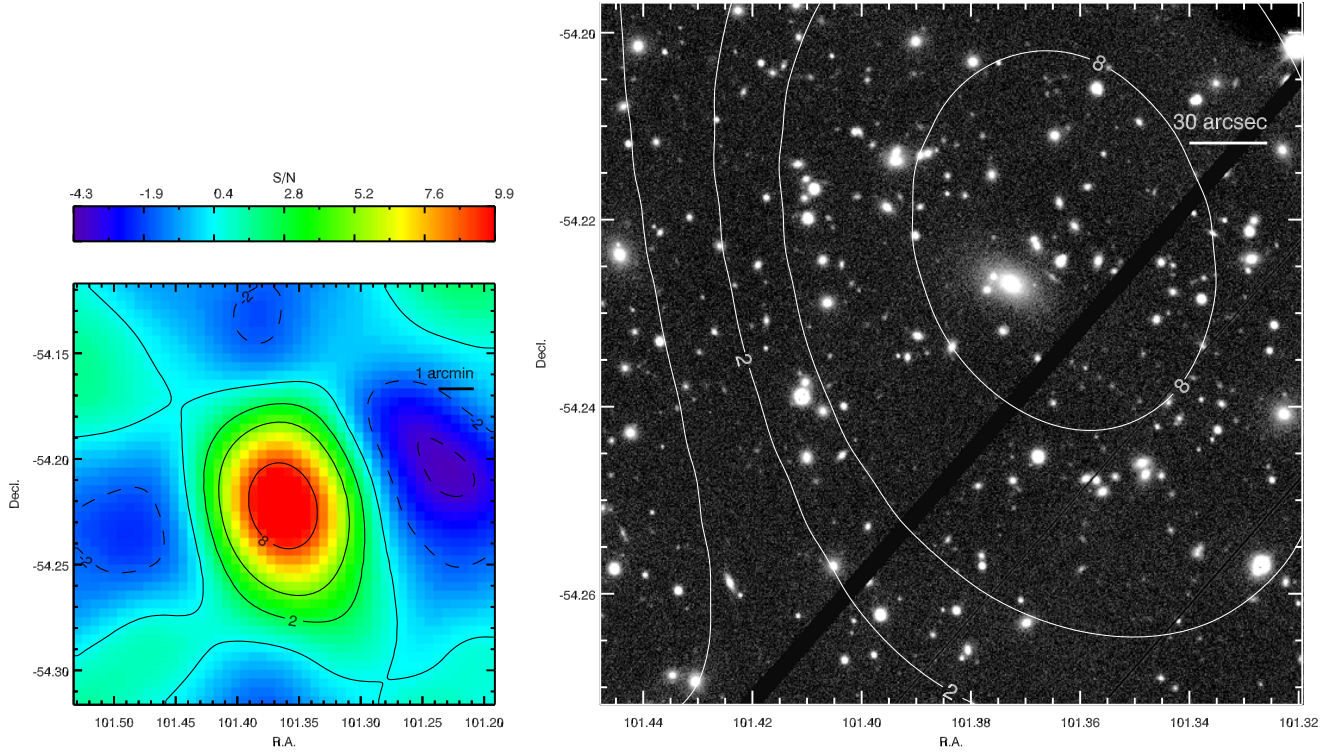


FIG. 22.— SPT-CL J0645-5413, also known as ABELL 3404, RXCJ0645.4-5413, and ACT-CL J0645-5413, at $z_{\text{spec}} = 0.167$. A VLT/FORS2 R image is shown in the optical/infrared panel.

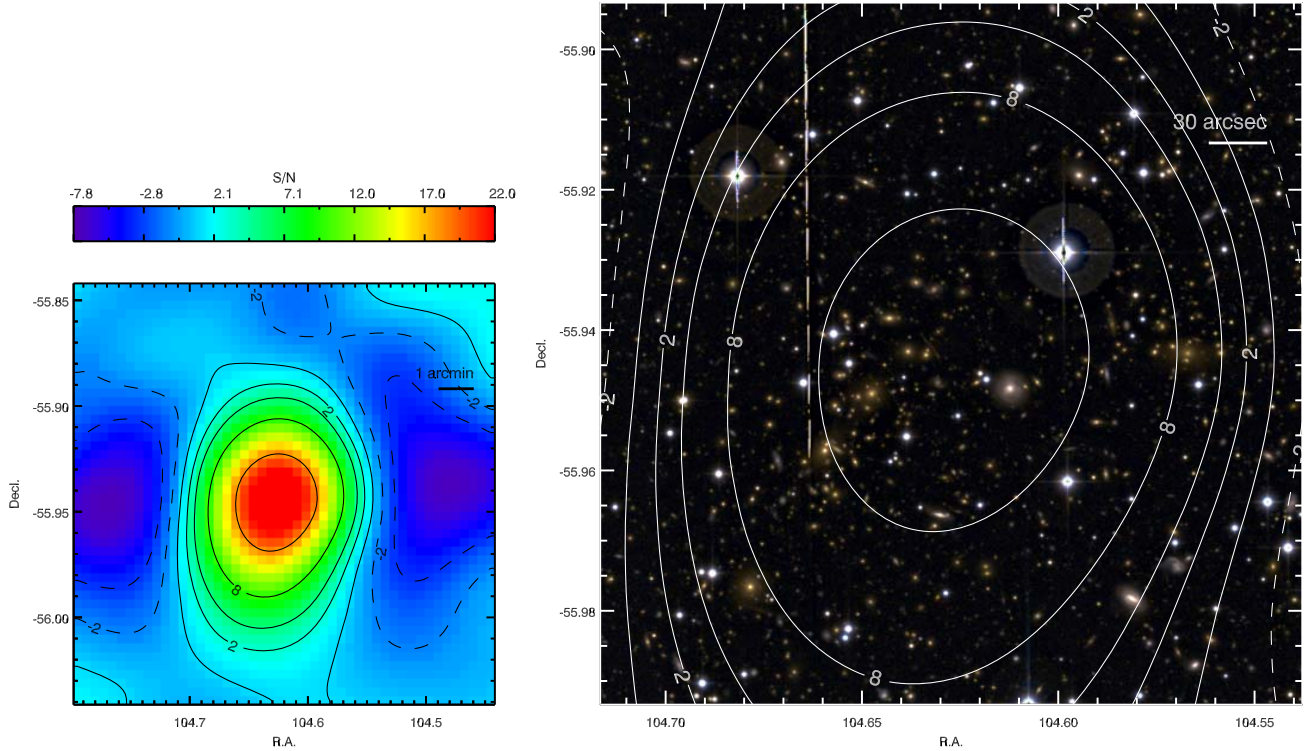


FIG. 23.— SPT-CL J0658-5556, also known as the Bullet Cluster, RXCJ0658.5-5556, and ACT-CL J0658-5557, at $z_{\text{spec}} = 0.296$. MPG-ESO/WFI R and V images are shown in the optical/infrared panel.

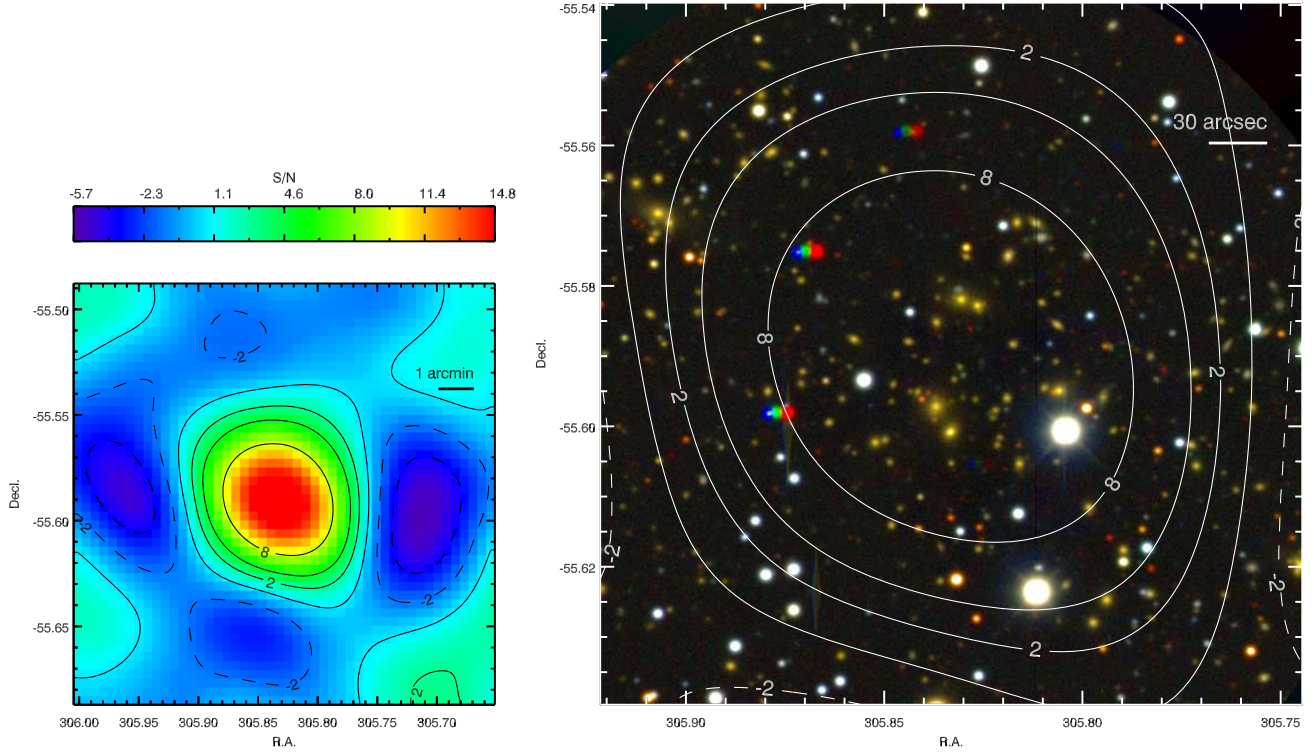


FIG. 24.— SPT-CL J2023-5535, also known as RXCJ2023.4-5535, at $z_{\text{spec}} = 0.232$. Magellan/LDSS3 *irg* images are shown in the optical/infrared panel.

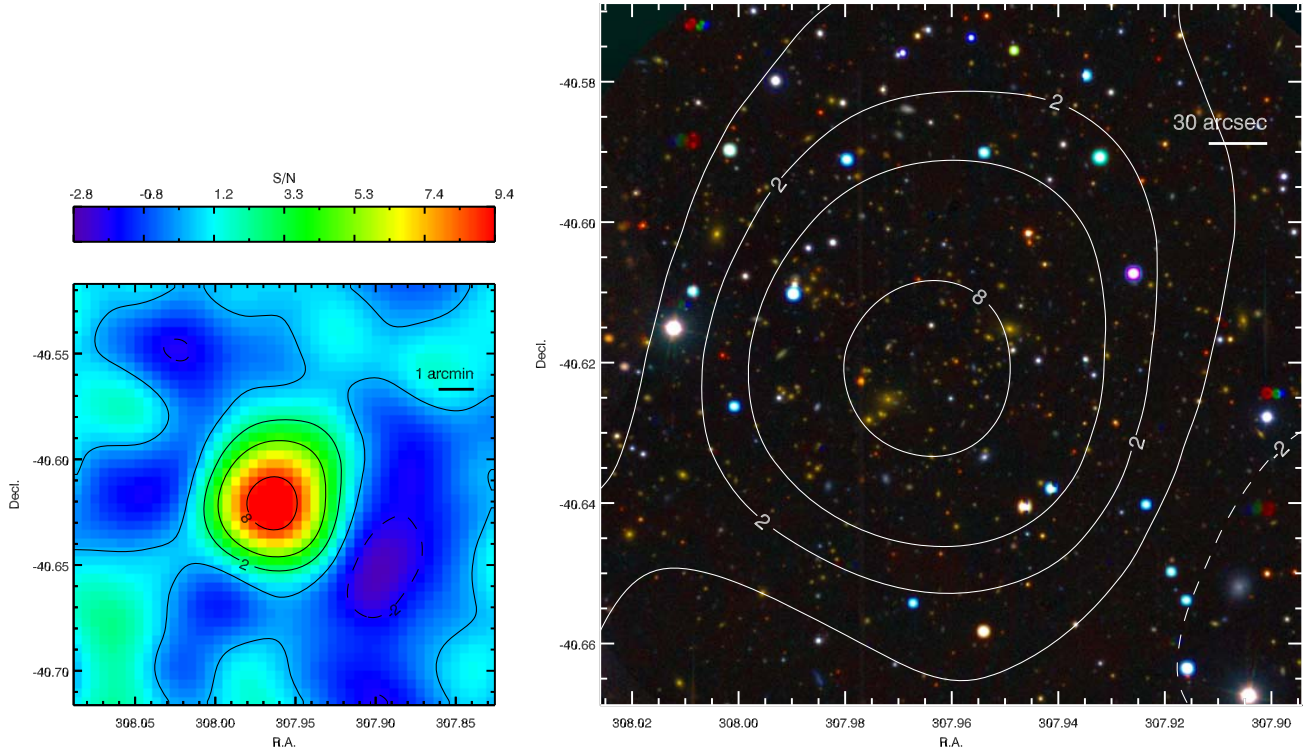


FIG. 25.— SPT-CL J2031-4037, also known as RXC J2031.8-4037, at $z_{\text{spec}} = 0.342$. Magellan/LDSS3 *irg* images are shown in the optical/infrared panel.

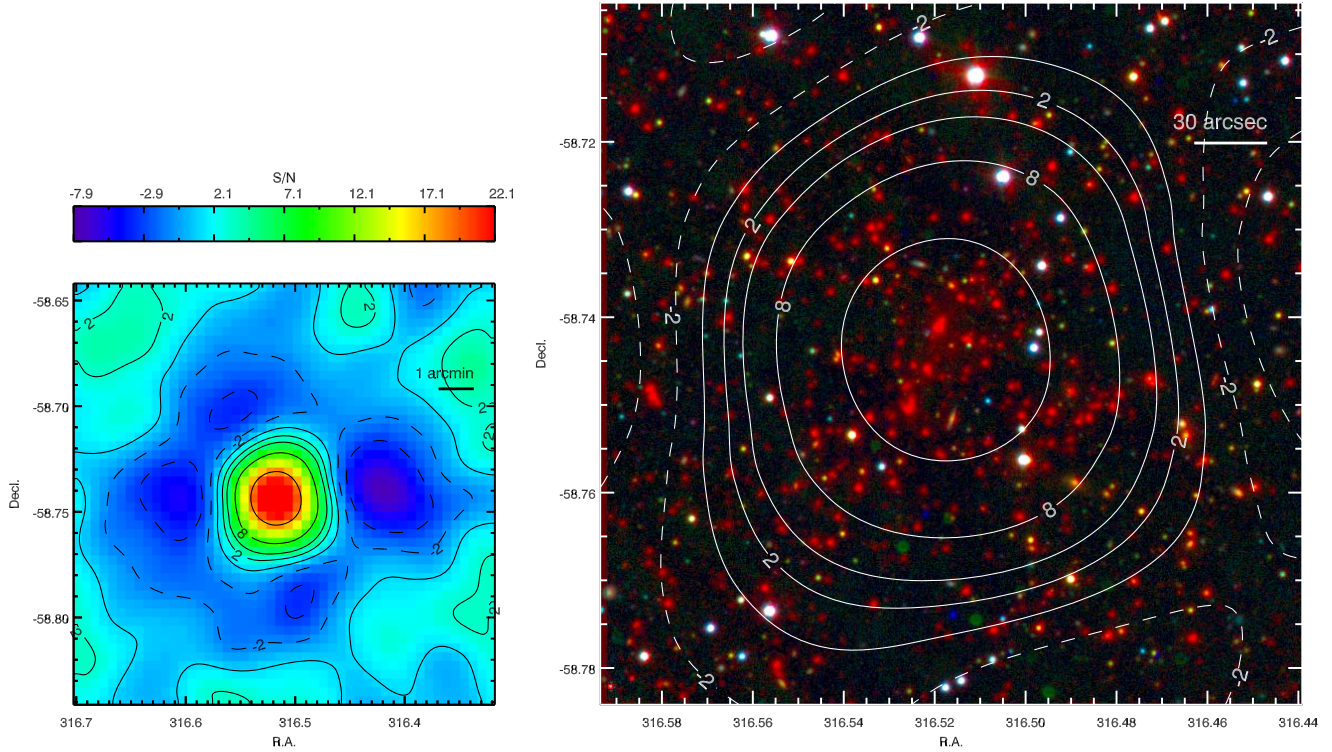


FIG. 26.— SPT-CL J2106-5844 at $z_{\text{spec}} = 1.133$. Spitzer/IRAC [3.6] and Magellan/LDSS3 ig images are shown in the optical/infrared panel.

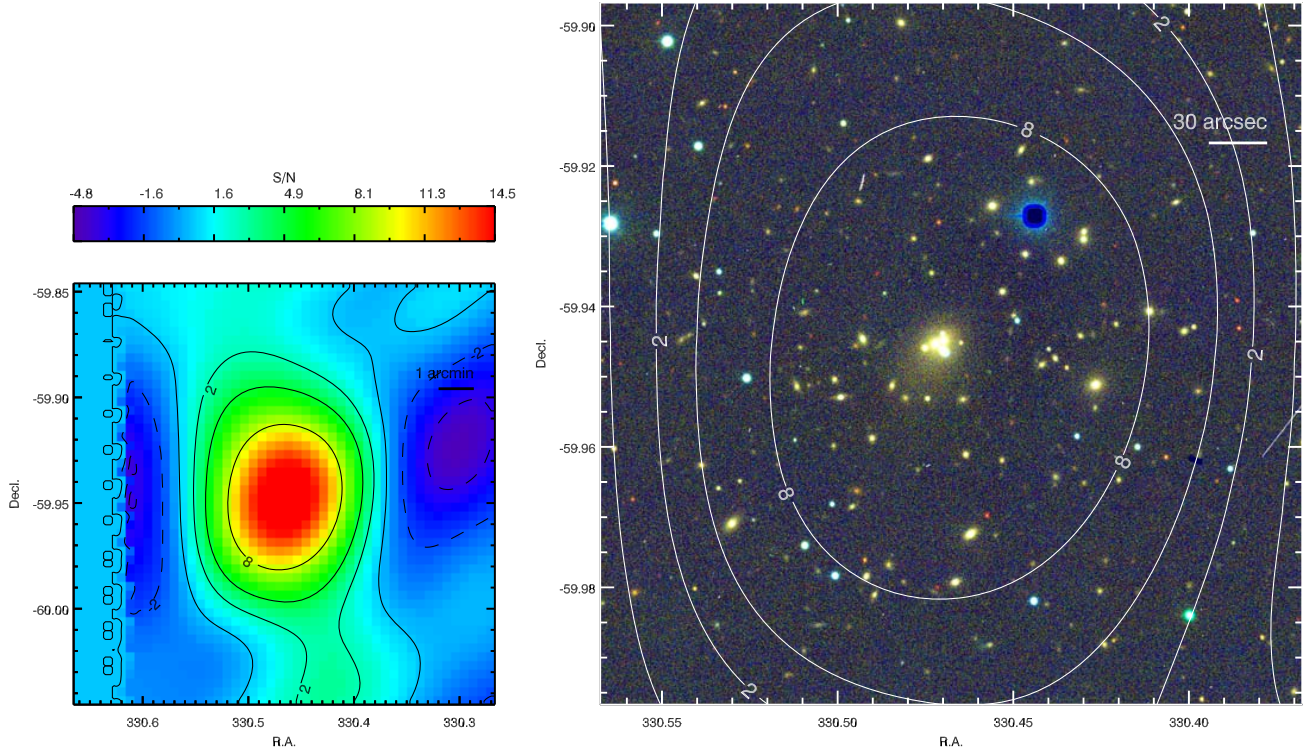


FIG. 27.— SPT-CL J2201-5956, also known as Abell 3827 and RXCJ2201.9-5956, at $z_{\text{spec}} = 0.098$. IMACS f/2 irg images are shown in the optical/infrared panel. This detection is at the eastern edge of the survey field.

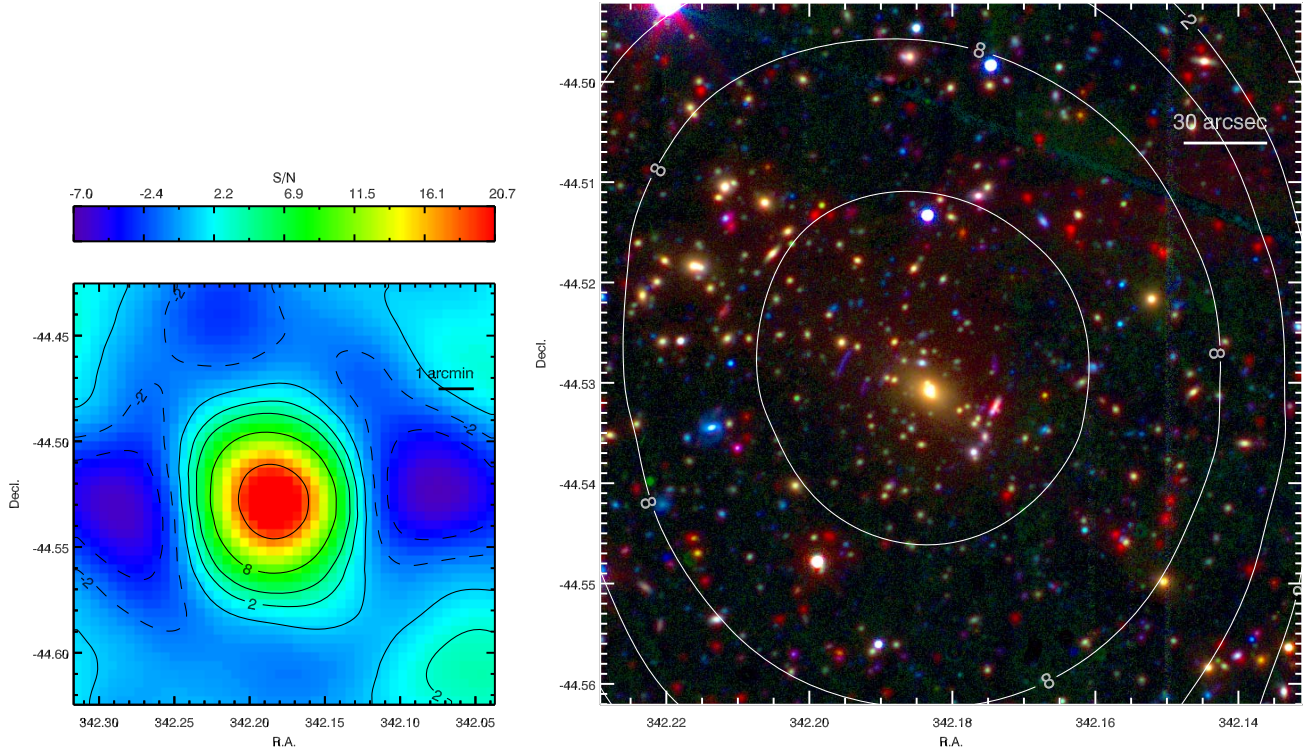


FIG. 28.— SPT-CL J2248-4431, also known as Abell S1063 and RXCJ2248.7-4431, at $z_{\text{spec}} = 0.348$. Spitzer/IRAC [3.6] and Magellan/LDSS3 *ig* images are shown in the optical/infrared panel.

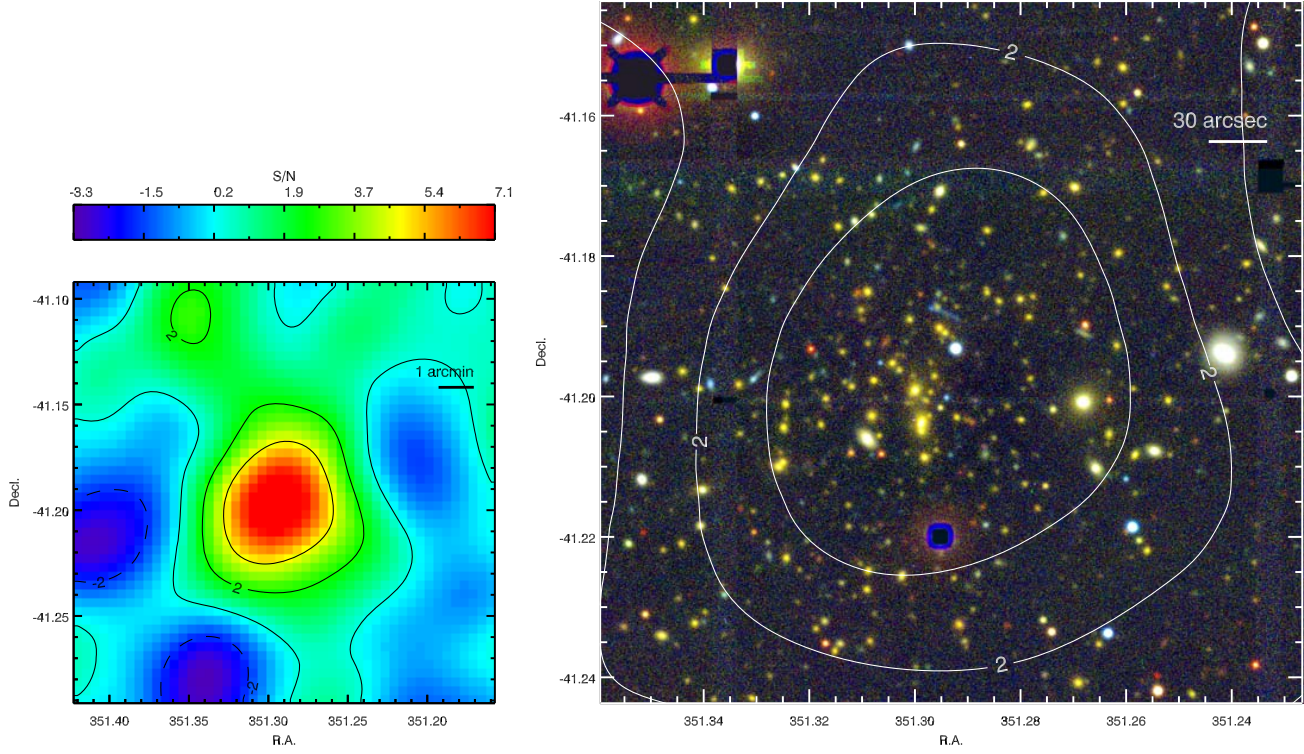


FIG. 29.— SPT-CL J2325-4111, also known as Abell S1121, at $z_{\text{rs}} = 0.37$. Blanco/MOSAIC-II *irg* images are shown in the optical/infrared panel.

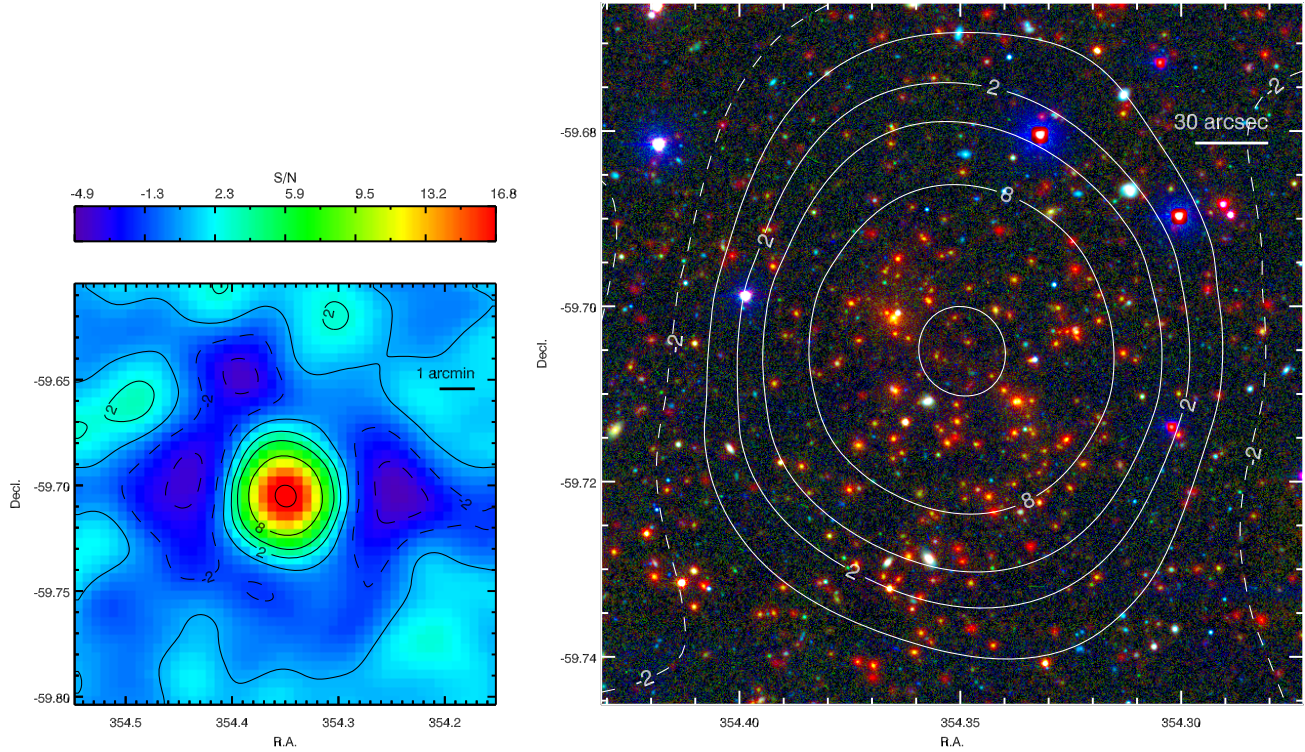


FIG. 30.— SPT-CL J2337-5942 at $z_{\text{spec}} = 0.775$. Spitzer/IRAC [3.6] and Magellan/IMACS f/2 *ig* images are shown in the optical/infrared panel.

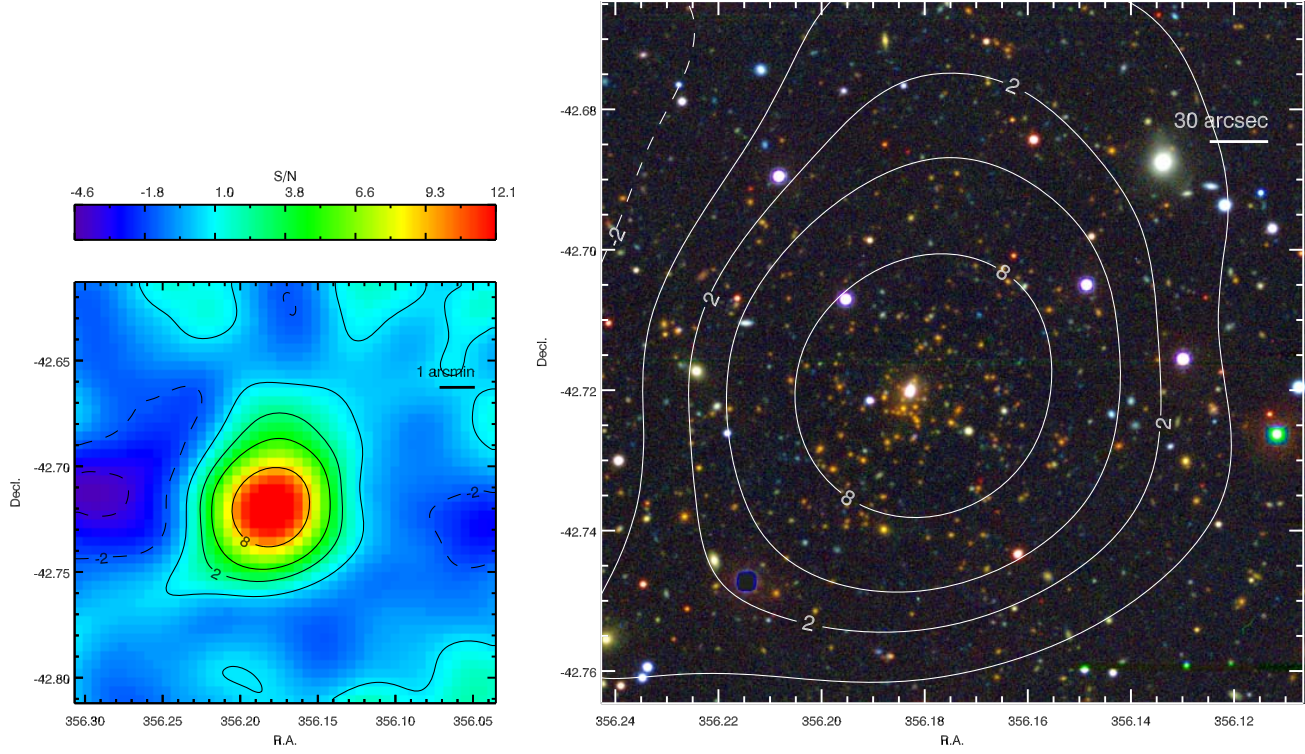


FIG. 31.— SPT-CL J2344-4243 at $z_{\text{rs}} = 0.62$. Blanco/MOSAIC-II *irg* images are shown in the optical/infrared panel.